

# CEBAF Program Advisory Committee Nine Proposal Cover Sheet

This proposal must be received by close of business on Thursday, December 1, 1994 at:

CEBAF

User Liaison Office, Mail Stop 12 B

12000 Jefferson Avenue

Newport News, VA 23606

## Proposal Title

Electroproduction of Kaons up to  $Q^2 = 3 \text{ (GeV/c)}^2$

## Contact Person

Name: Pete Markowitz

Institution: The University of Maryland

Address: Physics Department

Address: Experimental Nuclear Physics

City, State ZIP/Country: College Park, MD 20742

Phone: 301-405-6105

FAX: 301-314-9525

E-Mail → Internet: markowitz@cebaf.gov

Experimental Hall: A Days Requested for Approval: 23

Hall B proposals only, list any experiments and days for concurrent running:

## CEBAF Use Only

Receipt Date: 12/15/94

PR 94-108

By: P

## LAB RESOURCES REQUIREMENTS LIST

CEBAF Proposal No.: \_\_\_\_\_  
(For CEBAF User Liaison Office use only.)

Date: \_\_\_\_\_

(For CEBAF User Liaison Office use only.)

List below significant resources — both equipment and human — that you are requesting *from CEBAF* in support of mounting and executing the proposed experiment. Do not include items that will be routinely supplied to all running experiments, such as the base equipment for the hall and technical support for routine operation, installation, and maintenance.

Major Installations (either your equip. or new equip. requested from CEBAF)	Major Equipment

## Magnets

## Power Supplies

Targets	From
---------	------

## Detectors

## Electronics

## Computer Hardware

Other \_\_\_\_\_

### ***Data Acquisition/Reduction***

**Computing Resources:** \_\_\_\_\_

**Other**

**New Software:** \_\_\_\_\_

Appendix H1: HAZARD IDENTIFICATION CHECKLIST for Experiment # \_\_\_\_\_  
(Check all items for which there is anticipated need)

<b>Cryogenics</b> <input type="checkbox"/> beamline magnets <input checked="" type="checkbox"/> analysis magnets <input checked="" type="checkbox"/> targets type: <u>LH2</u> flow rate: _____ capacity: <u>.768 g/cm<sup>2</sup></u>	<b>Electrical equipment</b> <input checked="" type="checkbox"/> cryo/electrical devices <input checked="" type="checkbox"/> capacitor banks <input checked="" type="checkbox"/> high voltage <input checked="" type="checkbox"/> exposed equipment	<b>Radioactive/hazardous materials</b>  List any radioactive or hazardous/toxic materials planned for use: _____ _____
<b>Pressure vessels</b> <input type="checkbox"/> inside diameter <input type="checkbox"/> operating pressure <input type="checkbox"/> window material <input type="checkbox"/> window thickness	<b>Flammable gas or liquids</b> type: <u>LH2</u> flow rate: _____ capacity: _____  <b>Drift Chambers</b> type: <u>VDC</u> flow rate: _____ capacity: _____	<b>Solid Target materials</b> <input type="checkbox"/> Beryllium (Be) <input type="checkbox"/> Lithium (Li) <input type="checkbox"/> Mercury (Hg) <input type="checkbox"/> Lead (Pb) <input type="checkbox"/> Tungsten (W) <input type="checkbox"/> Uranium (U) <input checked="" type="checkbox"/> other (list below) <u><sup>12</sup>C</u> <u>CH<sub>2</sub></u>
<b>Vacuum vessels</b> <input type="checkbox"/> inside diameter <input type="checkbox"/> operating pressure <input type="checkbox"/> window material <input type="checkbox"/> window thickness	<b>Radioactive sources</b> Use: <input type="checkbox"/> permanent installation <input type="checkbox"/> temporary  type: _____ strength: _____	<b>Large mechanical structure/system</b> <input type="checkbox"/> lifting devices/carriages <input type="checkbox"/> motion controllers <input type="checkbox"/> scaffolding or <input type="checkbox"/> elevated platforms
<b>Lasers</b> type: _____ wattage: _____ class: _____  <b>Installation:</b> <input type="checkbox"/> permanent <input type="checkbox"/> temporary  <b>Use:</b> <input type="checkbox"/> calibration <input type="checkbox"/> alignment	<b>Hazardous chemicals</b> <input type="checkbox"/> cyanide plating materials <input type="checkbox"/> scintillation oil <input type="checkbox"/> PCBs <input type="checkbox"/> methane <input type="checkbox"/> TMAE <input type="checkbox"/> TEA <input type="checkbox"/> photographic developers <input type="checkbox"/> other (list below) _____ _____	<b>General:</b>  <b>Experiment Class:</b> <input checked="" type="checkbox"/> Base Equipment <input type="checkbox"/> Temp. Mod. to Base Equipment <input type="checkbox"/> Permanent Mod. to Base Equipment <input type="checkbox"/> Major New Apparatus  Other: _____ _____



# Electroproduction of Kaons up to $Q^2=3 \text{ (GeV/c)}^2$

C.C. Chang, P. Markowitz

*University of Maryland, College Park, Maryland*

S. Frullani, M. Iodice

*INFN - Sanita', Italy*

O.K. Baker

*Hampton University, Hampton, Virginia*

Hall A Collaboration Proposal

*CEBAF, Newport News, Virginia*

*The George Washington University, Washington D.C.*

*MIT, Cambridge Massachusetts*

*The Rutgers University, Piscataway, New Jersey*

*The University of Virginia, Charlottesville, Virginia*

*Tohoku University and KEK, Tokyo, Japan*

*University of Regina, Canada*

*Yerevan Physics Institute, Yerevan, Armenia*

*University of Georgia, Athens Georgia      INFN - Lecce, Italy*

*INFN - Bari, Italy*

December 20, 1994

Current:	Cryogenic Targets:	Beam Energies:	Beam Time:
100 $\mu$ A	LH2 10 cm	3.6, 4.0, 4.8, 5.2, 6.0 GeV	560 hours

## Abstract

We propose to measure the kaon electroproduction cross section, picking specific reaction channels via a separation of response functions in the exclusive  $H(e,e'K^+)$  reaction. Current experimental knowledge is unsatisfactory with no systematic separation of the response functions. Multi-parameter models based on hadron dynamics (QHD) have attempted to explain the existing data, but a wider kinematical region has to be accessed in order to constrain the models and the  $g_{KN\gamma}$  coupling constants.

Over a range in  $Q^2$ ,  $W$ , and  $t$ , the separation of three of the four unpolarized response functions will be performed. The longitudinal and transverse response functions will be separated through the detection of kaons along the direction of the virtual photon, where only these terms contribute to the cross section. For each  $Q^2$  kinematic three different points in  $t$  will be measured. From the extrapolation in  $t$  of the longitudinal term, the electromagnetic form factor of the kaon will, in principle, be determined. The separation of the longitudinal-transverse interference term will also be performed for selected kinematics. In a quark model description, the measurement of the longitudinal-transverse interference term is sensitive to the magnitude of the quark transverse momentum. The  $t$ -dependence of the full cross section will also be investigated to enlarge the accessed kinematical region, reaching large values of  $|t|$  covering the transition from a semiphenomenological description in terms of mesons and baryons to a pQCD-based description in terms of quarks (or diquarks).

The square of the 4-momentum transferred by the electron will cover the range  $1.5 \leq Q^2 \leq 3 \text{ (GeV/c)}^2$ , the hadronic 4-momentum transfer squared will cover the range  $-0.3 \geq t \geq -3.0 \text{ GeV}^2$ , and the invariant mass will cover the range  $1.8 \leq W \leq 2.2 \text{ GeV}$ . The measured cross sections will be compared to both hadronic and subnucleonic reaction models. This will considerably extend the present electroproduction data. Incident beam energies from 3.6 to 6 GeV will be utilized, along with the Hall A spectrometers. It should be emphasized that with 560 hours, this experiment will provide a consistent data set in a wide region of  $Q^2$ ,  $W$ , and  $t$ , which cannot be accessed elsewhere at CEBAF.

# 1 Introduction

## 1.1 Physics Motivation

The current situation for kaon photo- and electroproduction is unsatisfactory, both from the experimental and theoretical point of view. Measurements of the  $\gamma + p \rightarrow K^+ + Y$  and  $e + p \rightarrow e' + K^+ + Y$  ( $Y = \Lambda, \Sigma^0$ ) reactions have been limited by short lifetimes ( $c \cdot t_K = 370$  cm,  $c \cdot t_\Lambda = 8$  cm), small production rates (an order of magnitude smaller than for pions) and high thresholds ( $E_{th}(K\Lambda) = 911$  MeV,  $E_{th}(K\Sigma^0) = 1.05$  GeV). Knowledge from photoproduction data (reviewed, e.g., in ref. [1]) has not improved much in twenty years. The cross sections are known with an accuracy of about 10%. The polarizations are determined only for few points in the  $\Lambda$  production with errors of 25% to 50%. The photon energy range is limited to  $0.9 \leq E_\gamma \leq 1.4$  GeV (a few additional points were measured [2, 3] at a fixed momentum transfer  $t = -0.147$  GeV<sup>2</sup> in the energy range  $E_\gamma = 1.05 - 2.2$  GeV).

$\Lambda$ -electroproduction data are more sparse and have been measured only at higher energies (invariant mass energies  $W > 2.1$  GeV).[4, 5, 6] The experimental information on  $\Sigma^0$  production is even more scarce. In the following we will focus on the  $\Lambda$  production, but all proposed measurements on the proton will also allow simultaneous measurement of the  $\Sigma^0$  channel.

There are also theoretical problems in understanding the electroproduction process. In the low energy region various semiphenomenological descriptions in terms of mesons and baryons have been used. The hadronic field theories do not explicitly contain the quark degrees of freedom, but provide an effective description of the dynamics in the low- and intermediate-energy range. The semiphenomenological parameters of the theory (strong coupling constants, transition magnetic moments) are fit to the available photoproduction data using transition amplitudes based on the tree level Feynman diagrams.

In general, phenomenological  $\chi^2$  parameter fits are not unique due to the large number of coupling constants (up to 12 effective parameters are used; four of them enter the Born terms and the rest are associated with the resonance terms[7]) and the experimental uncertainties and limited kinematical region that has been so far explored. Hence, many sets of the parameters can fit the data equally well in the photoproduction channel. The various fits, however, differ when extrapolated outside the kinematics used in the fitting procedure ( $E_\gamma \geq 1.4$  GeV, virtual photons). The fits are also not equivalent from the point of view of the theoretical interpretation.

First of all there is disagreement between the values of coupling constants derived from the purely hadronic processes and from the available photoproduction data. The value of the leading coupling constant  $g_{K\Lambda p}/\sqrt{4\pi}$  is in the range from -1 to -3 in most photoproduction models, while its accepted hadronic value is about -4[8], in agreement with the broken SU(3) prediction[1]. This discrepancy is resolved by inclusion of the t-channel  $K_1$  resonance state with  $J = 1^+$  ( $M=1280$  MeV,  $\Gamma=90$

MeV) but only at the price of a very strong  $K_1\Lambda p$  coupling[1].

Thus, the situation in the theory of photo- and electroproduction of strange mesons is rather complicated. A variety of models (see e.g. review in [9]) differing in contributing resonances and coupling constants (including the leading ones  $g_{K\Lambda p}$  and  $g_{K\Sigma p}$ ) fit the available photoproduction data equally well - Figure 1. The  $\Lambda$

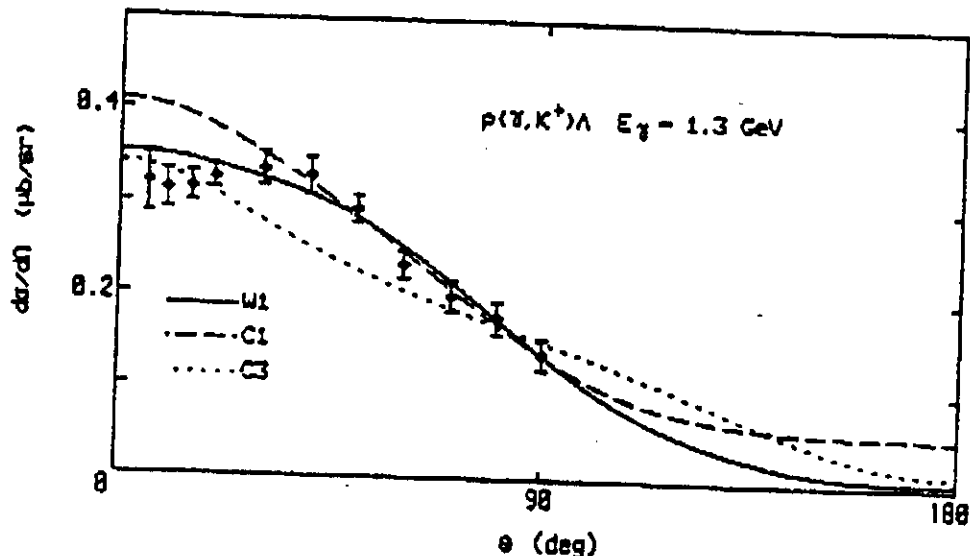


Figure 1: The photoproduction cross section calculated with different models.

polarization data are more selective in this respect. Here predictions of various models differ significantly; nevertheless, only the models based on the Born diagrams alone can be rejected.[9]

In this proposal, we concentrate on exclusive kaon production. The present proposal is based on two previously submitted proposals [PR-93-014 and PR-93-047]. One of them focussed mainly on the Deep Inelastic Region, requiring 6 GeV incident beam energy, and was treated as a LOI by the PAC. The other was specifically intended to be carried out with a new spectrometer[14] which was not funded; that spectrometer was intended to go out-of-plane, allowing a complete separation of the four unpolarized response functions.

Philosophically, with the construction of a high energy, high quality, high duty factor, and high intensity electron beam facility at CEBAF, it becomes possible and pertinent to investigate the properties of quarks inside a nucleon in an exclusive  $(e,e'q)$  experiment similar to the  $(e,e'p)$  or the  $(p,2p)$  studies for nucleons inside a nucleus.[10] Such an exclusive measurement samples (*i.e.*, isolates) a specific channel of the deep inelastic inclusive cross section. However, before the struck quark reaches the detector, it turns itself into color singlet hadrons. Study of the properties of the



hadron system produced following the deep inelastic scattering may give information on the mechanisms by which the nucleon's partons rearrange themselves into the observable hadrons after the primary scattering. These mechanisms must be related to the forces that bind partons into the original nucleon, and may shed insight as to why no parton has yet been observed as a separate entity.

Due to the lack of data, attempts to investigate the problem of electromagnetic production of strangeness on a subnucleon (quark) level are only beginning. Only recently has the photo- and electroproduction reaction been calculated in terms of the hard scattering model of Brodsky and Lepage[11], and of the diquark mechanism[12].

The electroproduction of kaons at CEBAF energies may also give insight about the transition to quark degrees of freedom: In a naive quark-parton model, and assuming the string fragmentation model, the production of a  $K^+$  can be considered to occur in two steps. First, a  $u$  quark is struck. As the  $u$  quark moves away from the target remnants, the color string between the  $u$  quark and the remnants breaks, producing an  $s\bar{s}$  quark pair. If there is additional energy stored in the color strings, more  $q\bar{q}$  pairs will result producing more hadrons. Because of the "low" energy in the CEBAF beam and the "high" masses of the kaon and the hyperon which are produced, the particle multiplicity will usually be low (as opposed to, say pion electroproduction). For those events with only two particles in the final state (a kaon and a hyperon such as the  $K^+$  and  $\Lambda$  for example), the transverse momentum of the produced kaon with respect to the 3-momentum transfer should be equal to the transverse momentum of the struck quark, or the primordial  $k_T$ . In this sense the dynamics of the struck quark are "preserved." As the incident electron energy increases beyond the range available at CEBAF, the particle multiplicity will also increase, meaning the  $K^+$  and  $\Lambda$  would only be part of the jet fragments.

## 1.2 Experiment Goals

The proposed experiment can be divided in three parts:

i) The separation of the longitudinal and transverse response functions through the detection of high momentum kaons along the direction of the virtual photon. For every  $Q^2$  kinematic, three central settings in  $t$  (and  $W$ ) will be measured. [The data can be more finely binned in  $t$  within the acceptance of the spectrometers.] The main goal of this part is the determination of the electromagnetic form factor of the kaon up to  $Q^2 = 3.0 \text{ (GeV/c)}^2$  from the  $t$ -dependence of the longitudinal term.

ii) The separation of the longitudinal-transverse interference term which, in a quark model description, gives information on the magnitude of the transverse momentum of quarks.

iii) The  $t$ -dependence of the full cross section up to large values of  $|t|$  where the transition from a semiphenomenological description in terms of mesons and baryons to a regime in which the theoretical approach based on quarks or diquarks description of the elementary process is applicable.

The experiment will provide a considerable set of data over a large kinematical region in  $W$ ,  $Q^2$ , and  $t$ , placing severe constraints on the models used to reproduce the data. In particular, important parameters such as the  $g_{K\Lambda p}$  coupling constant used in semiphenomenological models based upon hadron dynamic (QHD) formalism, can be much better established. Additionally the transition region to a more fundamental description of the reaction in terms of quarks can be identified, as well as determining which among the various proposed “pure quark” or “diquark” models has better reproducibility.

### 1.3 The Hall A Spectrometers

The accuracy of the HRS2 spectrometers in Hall A is ideal for these measurements since systematic uncertainties are magnified in the extraction of the response functions. More specifically, good angular resolution is required to accurately extract small amplitudes; the angular resolution and momentum resolution both enable the accurate kinematics binning event-by-event. The spectrometer acceptances should be flat to allow good binning of the data as a function of  $t$ .

The long flight path of the HRS2 means that the kaon survival fraction ranges between 10–35% for our kinematics, but the same flight path is responsible for the success of the time-of-flight particle identification. The missing mass resolution of the HRS2 will also cleanly separate  $\Lambda$ ,  $\Sigma^0$  and  $\Lambda(1405)$  final states from the continuum or higher resonances. [The  $\Lambda(1405)$  resonance has not been produced in photo-production reactions; the electroproduction data[13] are poor.]

The experiment can only be carried out in Hall A. Hall B, while tempting because it would enable one to take a large volume of phase space in one bite, does not have the particle identification capability at high momenta required by this experiment (in the CLAS identifying kaons with momenta  $\geq 2.0$  GeV/c is challenging). This experiment, while mapping out a large area of phase space not previously measured, also concentrates on high momentum, high invariant mass, and minimum  $|t|$  (i.e., the kaon-virtual photon angle=0), thereby focussing the kinematics on (relatively) forward scattering angles. This means that the large solid angle afforded by the CLAS does not buy much. Because of the high kaon and electron momenta, the SOS in Hall C is not suitable for this experiment.

The remainder of the proposal is split as follows: Section 2 defines the kinematic variables, discusses the hadronic and quark models for the cross section, estimates the behavior of the cross section as a function of  $Q^2$ ,  $W$ , and  $t$ , and provides physics details on the experiment goals. Section 3 lists the kinematics, rate estimates, cross sections and run times. Section 4 describes the particle identification and error analysis, and Section 5 summarizes the beamtime request and gives the experimental runplan.

## 2 Observables, Physics Models and Experiment Goals

### 2.1 Kinematical Variables and the Cross Section

The definitions of the kinematical variables are given for the reaction  $e + N \rightarrow e' + K + X$ . The five 4-momenta involved are:

$$\begin{aligned} e &= (E, \vec{e}) \text{ for the incident electron} \\ e' &= (E', \vec{e}') \text{ for the scattered electron} \\ N &= (M, \vec{0}) \text{ for the target nucleon} \\ K &= (E_K, \vec{k}) \text{ for the produced kaon} \\ X &= (E_X, \vec{x}) \text{ for the unobserved residual system.} \end{aligned}$$

A few Lorentz invariants and other kinematic variables are defined below as:

$$\begin{aligned} \gamma_v^2 &= (e - e')^2 = -Q^2 \\ \nu &= E - E' \\ \epsilon &= [1 + 2\frac{\nu^2 + Q^2}{Q^2} \tan^2 \frac{\theta_e}{2}]^{-1} \\ s &= (\gamma_v + N)^2 = W^2 \\ t &= (\gamma_v - K)^2 \\ x_B &= Q^2 / 2M\nu \\ y &= \nu / E \\ z &= E_K / \nu \\ M_X^2 &= (e - e' + N - K)^2 \end{aligned}$$

The differential cross section can be expressed as:

$$\frac{d^3\sigma}{dE' d\Omega_{e'} d\Omega_K} = \Gamma \cdot \frac{d\sigma_v}{d\Omega_k}$$

$\Gamma$  is the virtual photon flux, given by:

$$\Gamma = \frac{\alpha}{2\pi^2} \frac{E'}{E} \frac{s - M^2}{2MQ^2} \frac{1}{1 - \epsilon}$$

The cross section for single kaon production by virtual photons is given by

$$\frac{d\sigma_v}{d\Omega_k} = \frac{d\sigma_T}{d\Omega_k} + \epsilon \cdot \frac{d\sigma_L}{d\Omega_k} + \epsilon \cdot \frac{d\sigma_{TT}}{d\Omega_k} \cdot \cos(2\phi) + \sqrt{2\epsilon(\epsilon + 1)} \cdot \frac{d\sigma_{LT}}{d\Omega_k} \cdot \cos \phi$$

where  $\phi$  is the angle between the kaon production plane and the electron scattering plane, and  $\epsilon$  is the virtual photon polarization parameter. The pieces correspond to the cross section for unpolarized transverse ( $\sigma_T$ ), longitudinally polarized ( $\sigma_L$ ), polarized transverse interference ( $\sigma_{TT}$ ), and polarized longitudinal-transverse interference ( $\sigma_{LT}$ ) kaon production by virtual photons and only depend on the variables

$Q^2$ ,  $s$ , and  $t$ . In order to separate all four pieces of the cross section ( $\sigma_T$ ,  $\sigma_L$ ,  $\sigma_{TT}$ , and  $\sigma_{LT}$ ), a spectrometer with out-of-plane detection capability is needed to determine the  $\phi$  dependence of the cross section. For the special case in which the kaon is detected along the direction of the virtual photon, the interference terms vanish and  $\sigma_L$  and  $\sigma_T$  can be separated using a minimum of two measurements at different values of the virtual photon polarization  $\epsilon$ .

## 2.2 Description and Analysis of the Models

In order to have clear information on the electroproduction process, a comprehensive data set of cross sections and the extracted response functions are needed over a large range of  $W$ ,  $Q^2$  and  $t$ . The kinematic region of this experiment covers a transition between "traditional" nuclear physics and the deep inelastic region. There are several competing pictures of the reaction. Two extreme approaches are used here to provide guidance: semiphenomenological hadrodynamical scattering and quark hadronization. Seeing whether the data can be reconciled with any of the models is one goal of the experiment. Although obtaining data at very small  $x_B$  would provide the most information on the quark momentum distribution, the SLAC data[15] show that quark degrees of freedom evidence themselves at values of  $Q^2$  as low as 1 (GeV/c)<sup>2</sup>.

Figures 2 through 4 show the  $Q^2$ ,  $W^2$ , and  $t$  dependence of the reduced cross section ( $\frac{d\sigma_T}{d\Omega_k} + \epsilon \cdot \frac{d\sigma_L}{d\Omega_k}$ ), using a relativistic hadron pole model.[16, 17, 7] The fall-off shown in the cross section with increasing  $Q^2$  can be explained by the behavior of the form factor. Note the  $W^2$  behavior is fairly flat essentially indicating independence of  $W$ , while the cross section increases with higher  $|t|$ . The model is based on an effective field chiral Lagrangian evaluated at the tree level.

The hadronic field theories (e.g., the quantum hadrodynamics QHD) do not explicitly contain the quark degrees of freedom, but they provide a suitable effective scheme for description of dynamics in a low and intermediate energy range. The QHD is properly relativistic and simply related to the covariant S-matrix formalism. The semiphenomenological parameters of the theory (such as the strong coupling constants and transition magnetic moments) are fitted to the available data, making use of the transition amplitudes based on the tree level Feynmann diagrams (figure 5). In the intermediate state the particles which can be present are: in the s-channel a proton (Born term) or other strangeless nucleon resonances (figure 5a); in the u-channel the hyperons  $\Lambda$  or  $\Sigma$  (Born) or other spin 1/2 hyperons (figure 5b); in the t-channel the  $K^+$  (Born) or kaon resonances (figure 5c).

A variety of models were examined which used such a diagrammatic approach; the differences being mainly different particles in the intermediate state and the values of coupling constants and transition magnetic moments. The parameters used for all the models result from fitting to the available photoproduction data (a few also include electroproduction data). A general code considered more than ten models[9] varying intermediate particles, coupling constants and transition moments, as well

as different form factors. Beyond reproducing the cross sections provided by the authors of the models, further analysis compared predictions for the exclusive electroproduction reaction in the channel  $K\text{-}\Lambda$  extending the kinematical region (out from the region where the model was fit to the data). The results show that the data is reproduced very well by two of the considered models (referred to as wjc2 and wjc4 coming from the parameters set II from [18] and [7] respectively). While wjc4 is more complete from the theoretical point of view and has a good reproducibility for different reaction channels (namely  $p(e,e'K)\Lambda$ ,  $p(e,e'K)\Sigma$  and  $p(e,e'K)\Lambda(1405)$ , model wjc2 more accurately reproduces the measured cross section in the exclusive channel  $p(e,e'K)\Lambda$ . For example, the existing data up to about  $Q^2 = 4 \text{ (GeV/c)}^2$  (collected in [19]) are reproduced by the model wjc2 (only slightly underestimated) while they are significantly underestimated at high  $Q^2$  by wjc4. In addition, the  $K\text{-}\Lambda$  data reported in [7] (where the wjc4 model is presented) are well described by wjc2 as well and, moreover, the  $t$ -dependence of the cross section is in better agreement with the data which suggest a decrease in the cross section with increasing  $|t|$ , as suggested by photoproduction data (and almost all the models considered). Finally,  $\sigma_{LT}$  and  $\sigma_{TT}$  data[4] are better reproduced by wjc2 than wjc4. The latter predicts rather large contributions of the interference terms not suggested by the data. Nevertheless, when compared to the poor accuracy of existing electroproduction data, both models can be considered consistent with the existing data even if for high  $Q^2$  wjc2 appears preferable.

Some of the models we have considered also include crossing (as do both wjc2 and wjc4) and duality (also included in wjc4). The crossing constraint relates reactions with particles in the initial or final state with reactions with antiparticles in the final or initial state (and vice versa) thus making crossing a symmetry of the  $S$  matrix. The duality constraint, based on the dual role of resonances in the  $s$  ( $u$ ) and  $t$  channel, is used to restrict the number of resonances considered in the intermediate states, resulting in a model which includes only the  $s$  and  $u$ -channel resonances along with the usual Born terms (including the  $K^+$  exchange in the  $t$ -channel required by gauge invariance).

The second approach describes the process in terms of quarks fragmenting into hadrons. The feasibility of studying the jet fragmentation processes at CEBAF was simulated using the Lund Monte Carlo code LEPTO.[20] The Lund string model is one of the phenomenological tools that is routinely used by high-energy physicists to describe the hadronization of quark and gluon jets. The applicability of this model at the beginning of the scaling region has been studied by Dietrich and Johnson,[21] and found to be useful.

Basically, the hadronization process as described by the Lund Monte Carlo code LEPTO consists of three distinct phases: (i) formation of an initial quark-parton system (for lepton scattering, the quark-parton system is a quark-diquark pair) which depends on quark distribution functions and is a function of Bjorken  $x_B$ ; (ii) fragmentation of the quark-parton system into primary hadrons where the fragmentation function depends only on  $z$ ; and (iii) decay of the unstable primary hadrons

into the observed particles. The fragmentation of produced partons into observable hadrons is performed within the LUND string hadronization model as implemented in JETSET.[22] The results of these simulations show that the features of jet production similar to those observed at high energies are present even at CEBAF energies.

### 2.3 The Kaon form factor

The separation of as many of the response functions as possible is essential in differentiating between hadronic and quark degrees of freedom. In the quark picture, the interaction with the virtual photons contributes mainly to the transverse cross section (see the discussion below). On the other hand, an enhancement of the longitudinal cross section at small  $t$  (the squared 4-momentum transfer to the unobserved residual system) could indicate the influence of quasifree scattering from the kaon, as has been seen in pion electroproduction. As in the case of the pion, the  $Q^2$  dependence of  $\sigma_L$  can then be used to determine the kaon form factor.[23, 24]

The knowledge of the electromagnetic structure of any complex particle, made of charged substructures, always has been essential in the comprehension of its structure in terms of behaviour of the more fundamental components. The electromagnetic form factor can be theoretically deduced from models describing the way elementary components aggregate to form complex structures. It depends only on the square of the four-momentum transfer to the particle by the electromagnetic probe. Electron-positron colliding beam experiments measure the form factor in the time-like region, generally via the production of a particle-antiparticle pair. The measurement of the form factor in the space-like region is straightforward for nucleons or nuclei as they can be used as free targets; only in these cases are the cross sections directly proportional to the absolute square of the form factor.

Particles (mesons and baryons) that can be produced in sufficient quantity to be used as secondary beams in large hadron accelerators can be scattered from atomic electrons to measure the form factor, but due to the small electron mass only low values of momentum transfer can be obtained. At large space-like momentum transfers, the only reaction that can give information on form factors is the electroproduction process. The extraction of the kaon form factor from the data requires effort both on the experimental and theoretical side, as in the case of the pion form factor[19, 25].

The existing measurements in the space-like region come from  $K$ - $e$  scattering [19, 26] and are limited to a maximum  $Q^2$  of  $0.1 \text{ (GeV/c)}^2$ . Figure 6 shows these data, along with a recent theoretical calculation[27]. The possibility of determining the kaon form factor through the electroproduction reaction relies on: i) the  $t$  diagram of Figure 5, in which the meson exchanged is the kaon (kaon pole diagram), dominating all the other diagrams near the unphysical value  $t = M_K^2$  and ii) this behaviour being strong enough at physical values of  $t$  to allow a smooth extrapolation from experimental points to  $t = M_K^2$ . Theoretical guidance is necessary in the extrapolation to exploit model-independent constraints and analytical properties of the amplitudes. Experimentally, precise measurements are required in

kinematical conditions favourable for the extrapolation (reaching as low as possible in  $|t|$  approaching the unphysical region). For a given  $Q^2$  and a given  $W$  there is a minimum value for the variable  $t$  in the physical region ( $t_{min}$ ) that corresponds to the kinematical condition in which the kaon is emitted in the same direction as the 3-momentum transfer. In Figure 7 the dependence of  $t_{min}$  on  $W$  for different values of  $Q^2$  is shown. We want to measure the longitudinal and transverse response functions with a Rosenbluth separation at four values of  $Q^2$ : 1.5, 2, 2.5 and 3 (GeV/c)<sup>2</sup> and a range of values of  $t$  for every  $Q^2$  measurement. In these measurements  $W$  varies between 1.8 and 2.2 GeV.

The models assume a form for the dependence on the invariant mass  $W$ . This experiment will determine the dependence of the separated response functions on  $W$ , providing the theoretical models with an additional constraint. Extracting the kaon form factor from the longitudinal response function is model dependent; extrapolation of the longitudinal response function in  $t$  is somewhat less so. If the data can be described by the model then it gives some confidence that the coupling constants are correctly known. The success (or failure) of the model to describe the data can be attributed in large degree to the knowledge of these coupling constants.

The kaon form factor is proportional to the square root of the longitudinal response function extrapolated to the kaon pole[25]:

$$F_K^2(Q^2) = F_K^2(Q^2, t)|_{t \rightarrow M_K^2} = \frac{(t - M_K^2)^2 \sigma_L}{N(t)}|_{t \rightarrow M_K^2}$$

where

$$N(t) = (-t)8cg_{KNY}^2[k^2 \sin^2 \theta_e \frac{1 + \epsilon \cos 2\phi}{2} + \epsilon \frac{(qE_K - \nu k \cos \theta_e)^2}{Q^2}]$$

According to some nuclear interaction models, the kaon form factor has been shown to dominate the longitudinal response function at the kaon pole.[7] Assuming the kaon pole does dominate the cross section for small  $|t|$ , then the kaon form factor can in principle be determined (if the coupling constants are also known).

Figure 8 shows the kaon form factor  $Q^2 F_K(Q^2)$ , as a function of  $Q^2$ , [27] along with the four points indicating the region to be explored in the present experiment. Also shown are other simpler Vector Mesons Dominance Model predictions which consider, the  $\phi$ - and  $\rho$ -mesons and predictions from the only available model based on a more fundamental microscopic approach[27]. Due to the model dependence and the extrapolation to the kaon pole, a prior analysis of the theoretical uncertainties in the kaon form factor is difficult. To illustrate, the extracted ratio  $(t - M_K^2)^2 \sigma_L / N(t)$  for two models has been extrapolated in  $t$  at  $Q^2 = 1.5$  (GeV/c)<sup>2</sup> and  $\langle W \rangle = 2$  GeV. Figure 9 shows the  $t$ -dependence (along with the projected uncertainties) according to model wjc2, along with the kaon form factor extrapolated to the pole ( $t = M_K^2$ ). As can be seen the longitudinal term is fairly flat and below the "correct" value of the squared form factor; i.e., the kaon-pole diagram does not dominate at small  $|t|$  approaching the unphysical region.

The situation is better if the analysis is done in the wjc4 model. In this case, as can be seen in figure 10, the kaon pole diagram dominates approaching the positive- $t$  region. A simple extrapolation obtains a reasonable value of the kaon form factor with a reasonable uncertainty (being half that of the SQUARED extrapolated form factor). Figure 11 shows the same analysis for kinematics at  $Q^2 = 2.5$  (GeV/c)<sup>2</sup>. The two extrapolations are differentiated only by modelling the data in the physical region; further these are not extreme cases, meaning that we also have analysed models more and less difficult to extrapolate.

## 2.4 Transverse Momentum of the Quark

Measurement of  $\sigma_{LT}$  will shed light on the processes which contribute to the interference cross section, as well as give information on the magnitude of the “apparent” transverse momentum of quarks which could result from effects such as the primordial transverse momentum, the initial and/or final state soft gluon radiations, and the initial and/or final parton showers.  $\langle \cos \phi \rangle$  is measured by subtracting measurements made left of the direction of the virtual photon ( $\phi = 180$ ) from measurements made right of the virtual photon ( $\phi = 0$ ), at the same  $Q^2$ ,  $W$ , and  $t$ .  $\langle \cos \phi \rangle$  is defined as:

$$\langle \cos \phi \rangle = \frac{\frac{d\sigma_v(\phi=0)}{d\sigma_K} - \frac{d\sigma_v(\phi=180)}{d\sigma_K}}{\frac{d\sigma_v(\phi=0)}{d\sigma_K} + \frac{d\sigma_v(\phi=180)}{d\sigma_K}}$$

If an electron scatters relativistically off a pointlike target, because of the helicity conservation, either (i)  $\sigma_T = 0$  and  $\sigma_L \neq 0$  if the pointlike target has spin 0, meaning  $R = \frac{\sigma_L}{\sigma_T} \rightarrow \infty$ , or (ii)  $\sigma_T \neq 0$  and  $\sigma_L = 0$  if the pointlike target has spin 1/2, or  $R = \frac{\sigma_L}{\sigma_T} \rightarrow 0$ . A small experimental value of  $R$  in the DIS region suggests that the longitudinal cross section is nonzero. Two possible sources for the longitudinal amplitudes are: (i) the initial (primordial) transverse momentum of the struck quark, and (ii) the higher-twist correction to the quark-parton model. The former is a pure kinematic effect and was predicted to give a negative contribution to the longitudinal-transverse (LT) interference asymmetry as:[28]

$$\langle \cos \phi \rangle \sim - \frac{(2k_T/Q) \cdot (2-y) \cdot (1-y)^{1/2}}{[1 + (1-y)^2]}.$$

The latter is a dynamic effect and was first predicted to give a positive contribution to the LT interference cross section as:[29]

$$\langle \cos \phi \rangle \sim (k_T/Q) \cdot (1-y)^{1/2}$$

More recently, realistic quark wavefunctions have been included which give the prediction of the behavior going as:[30]

$$\langle \cos \phi \rangle \sim 1/2(k_T/Q) \cdot \frac{(2-y)\sqrt{1-y}H_3}{x_B y^2 H_1 + (1-y)H_2}$$



Plotted in Figure 12 is the longitudinal-to-transverse interference asymmetry,  $\langle \cos \phi \rangle$  plotted as a function of  $z$ , the fraction of the energy transfer which ended up in the kaon.[30] Although the model uses more realistic quark wave functions, no intrinsic transverse momentum for the meson constituents is introduced. By prescaling pion data as well, the importance of the meson intrinsic transverse momentum can be estimated.

Figure 13 shows a LEPTO simulation of the yield versus  $\theta_{kq}$ , the angle (in the lab frame) between the kaon momentum and the momentum transfer. Note that these measurements will be centered at about 7 degrees, where about 15% of the total yield will be captured. Figure 14 shows the  $\phi$  azimuthal distribution from LEPTO, which predicts a  $\cos \phi$  dependence to the cross section, consistent with the interference terms,  $\sigma_{LT}$  and  $\sigma_{TT}$ , being small but nonzero. Cuts have been placed on the spectrum corresponding to the electron arm acceptances and the kaon arm angular acceptances.

## 2.5 Tests of pQCD, large $|t|$ kinematics

The study of exclusive reactions at large  $|t|$  provides a way to shed light on the interaction mechanism which occurs at short distances in hadronic matter, selecting a hard scattering regime of the reaction (in comparison with a diffractive mechanism that occurs at small  $|t|$  values). Recently theoretical predictions of exclusive photo- and electro-production reactions based on perturbative QCD[11] or on a QCD semiphenomenological diquark model have become available[12].

The kinematical region in which computations based on the diquark approach are applicable is within CEBAF capabilities ( $W \geq 2$  GeV) and this experiment will measure the angular distribution to values of  $|t| \leq 1.5$  (GeV/c)<sup>2</sup>, covering the transition between small and large  $|t|$  where different descriptions of the reaction should be applicable. Separating the response functions (at small  $|t|$ ) and measuring the full cross section at large values of  $|t|$  will provide more observables to compare with the theory and to give guidance if a discrepancy is found.

Figure 15 shows the available data near CEBAF energies (4 and 6 GeV photon energies) on the  $\Lambda$  and  $\Sigma^0$  photoproduction reaction together with the predictions of the pQCD model. Plotted is the cross section scaled by  $s^7$  versus the  $\cos \theta_{\gamma K}$ , the cosine of the opening angle between the kaon and the virtual photon which is proportional to  $t$ . The calculation is a leading twist calculation, using the Born approximation. The scattering is sensitive to the quark wavefunctions and assumes the scattering is from the valence quarks. The model calculates the hard scattering in the  $s$ -channel with real photons. As can be seen, the data do not agree with the calculation. At the forward channels, the  $t$ -channel can contribute (and at backward angles from the  $u$ -channel can contribute).

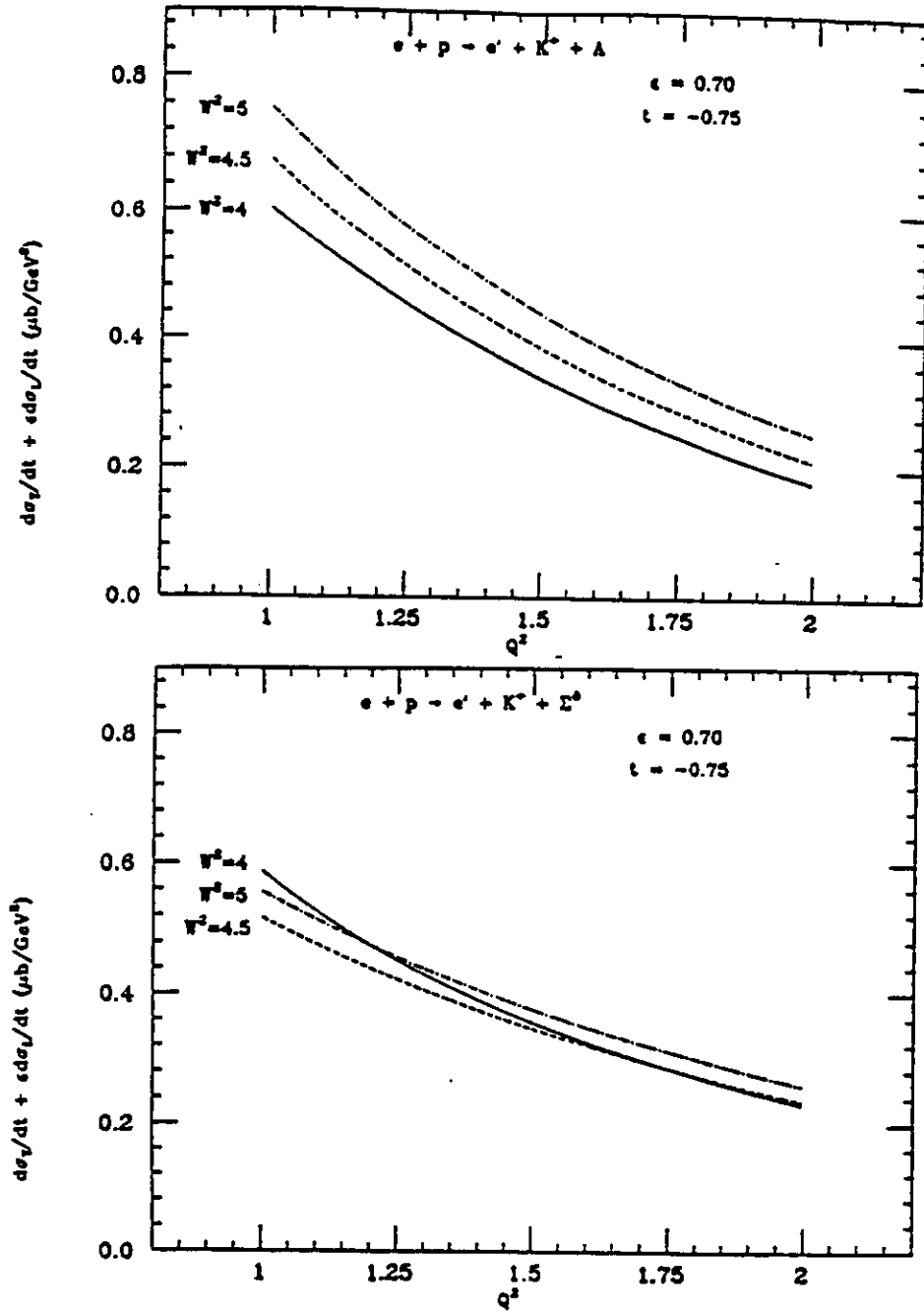


Figure 2: The  $Q^2$  dependence of the a)  $p(e, e' K^+) \Lambda$  and b)  $p(e, e' K^+) \Sigma^0$  cross sections. The curves are for  $t = -0.75 \text{ GeV}^2$ , and  $\epsilon = 0.70$ . The solid curve is  $W^2 = 4$ , the dashed curve is  $W^2 = 4.5$ , and the dotdash is  $W^2 = 5 \text{ GeV}^2$ .

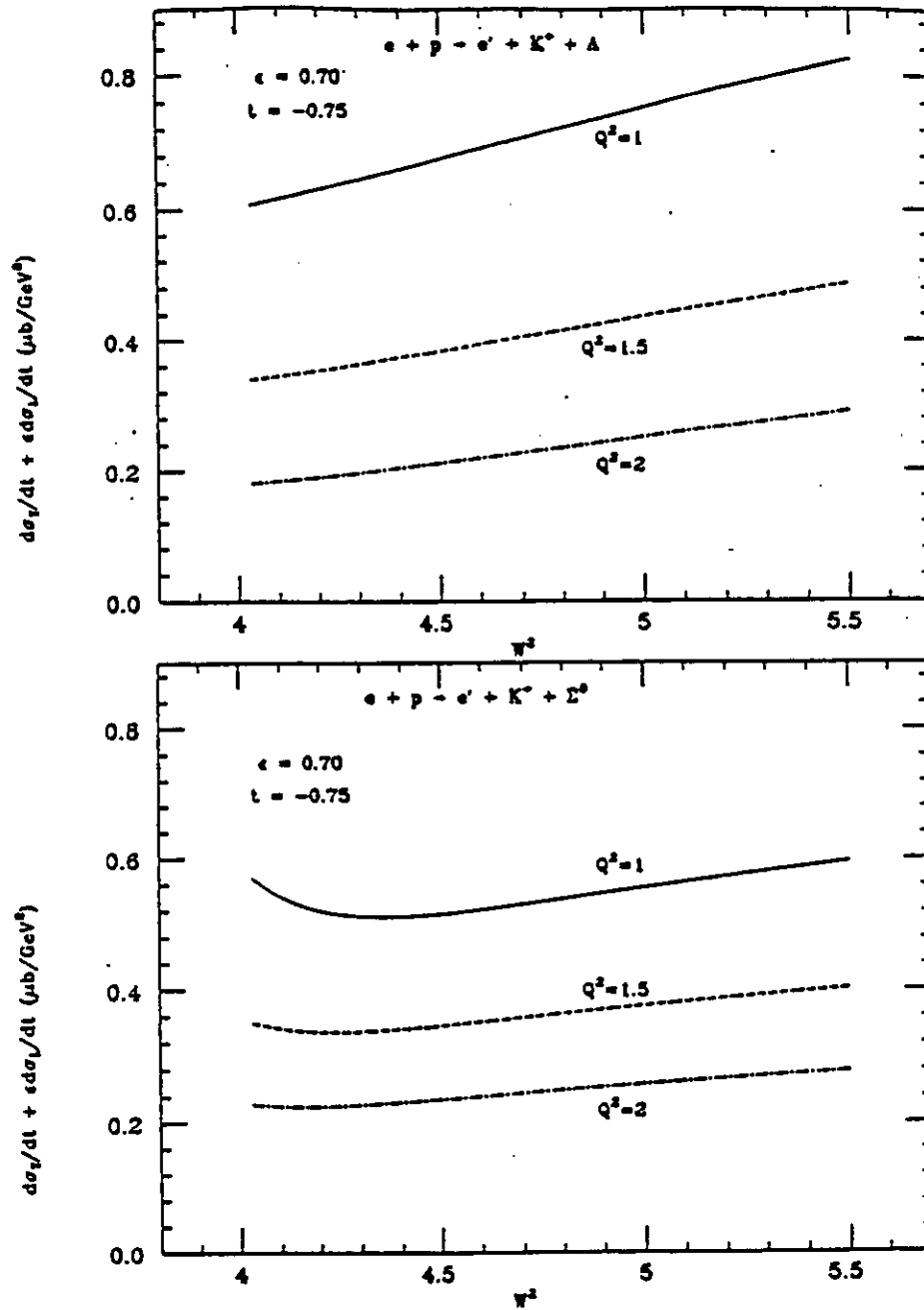


Figure 3: The  $W^2$  dependence of the a)  $p(e, e' K^+) \Lambda$  and b)  $p(e, e' K^+) \Sigma^0$  cross sections. The curves are for  $t = -0.75 \text{ GeV}^2$ , and  $\epsilon = 0.70$ . The solid curve is  $Q^2 = 1$ , the dashed curve is  $Q^2 = 1.5$ , and the dotdash  $Q^2 = 2(\text{GeV}/c)^2$ .

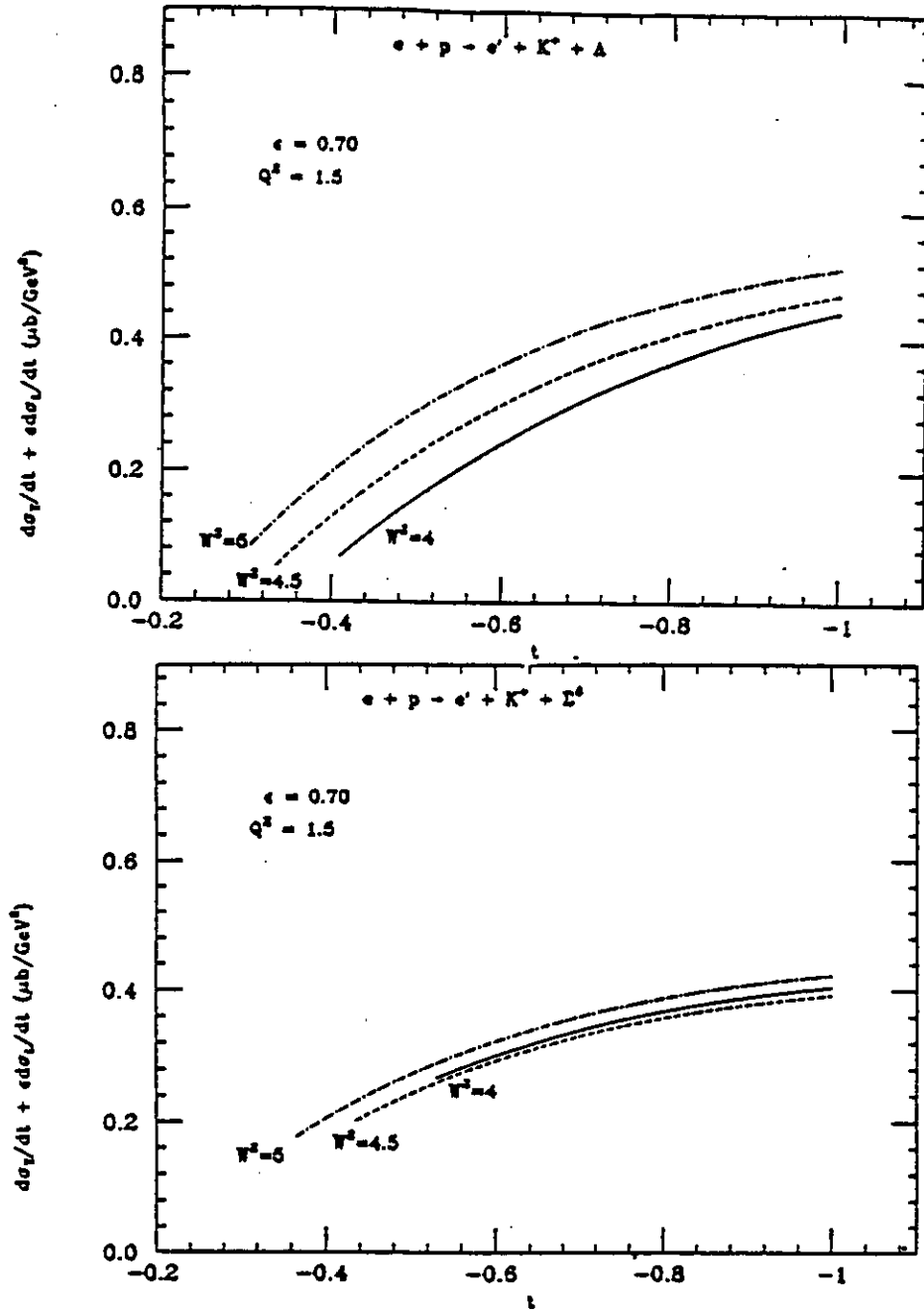


Figure 4: The  $t$  dependence of the a)  $p(e, e'K^+)\Lambda$   $p(e, e'K^+)\Sigma^0$  cross section. The curves are for  $Q^2 = 1.5$  ( $\text{GeV}/c$ ) $^2$ , and  $\epsilon = 0.70$ . The solid curve is  $W^2 = 4$ , the dashed curve is  $W^2 = 4.5$ , and the dotdash is  $W^2 = 5\text{GeV}^2$ .

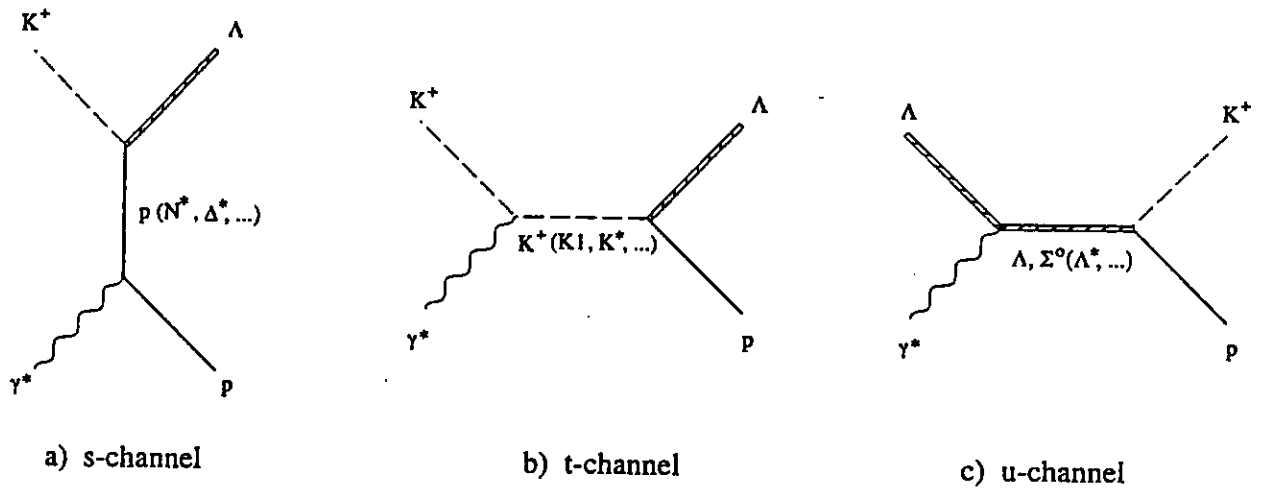


Figure 5: Tree level Feynman diagrams in kaon electroproduction. B stands for proton or nucleon resonance, S stands for a baryon with strangeness  $S=-1$ , and M for mesons.

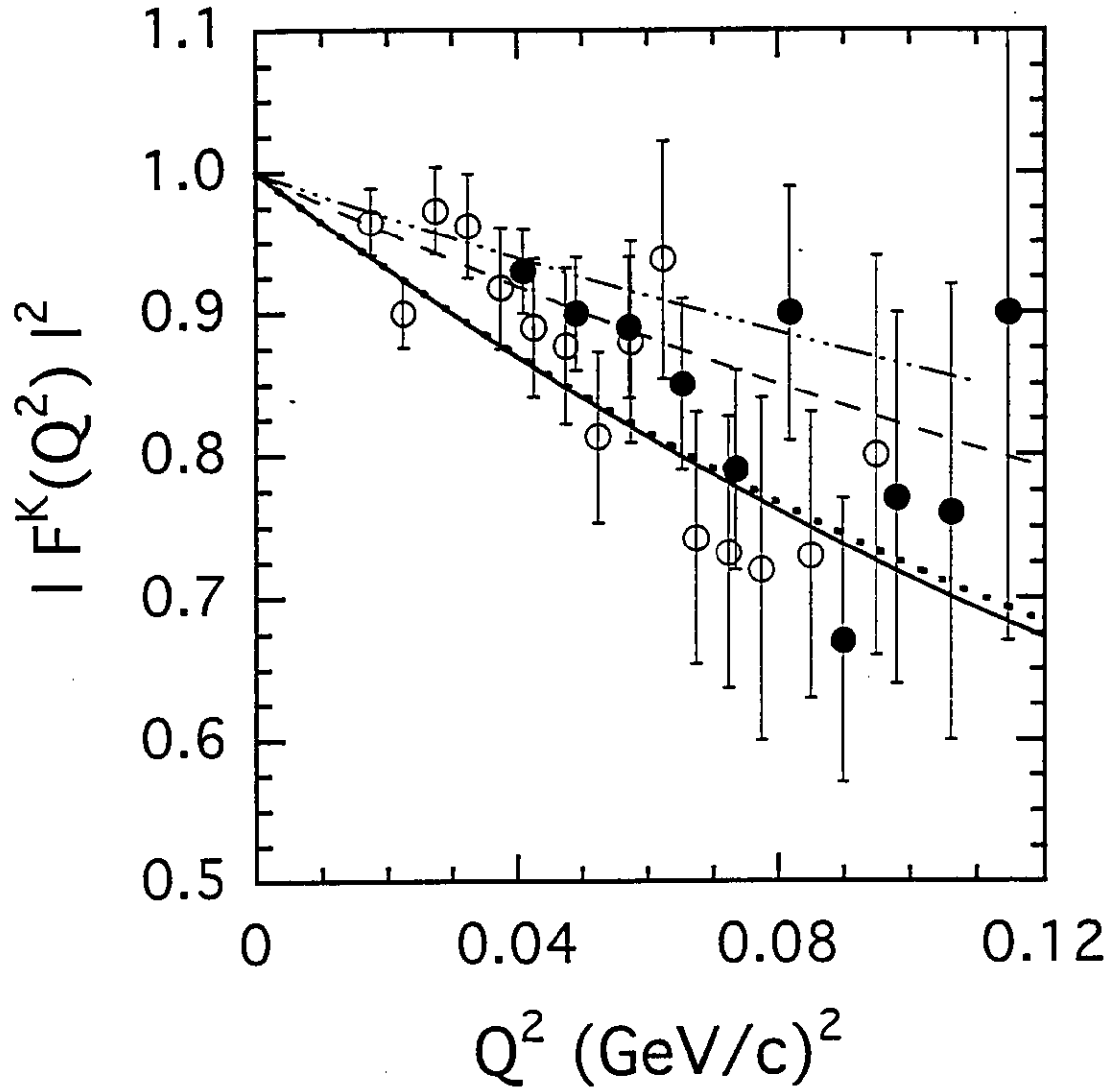


Figure 6: The Kaon form factor,  $F_K(Q^2)$ , plotted as a function of  $Q^2$ .

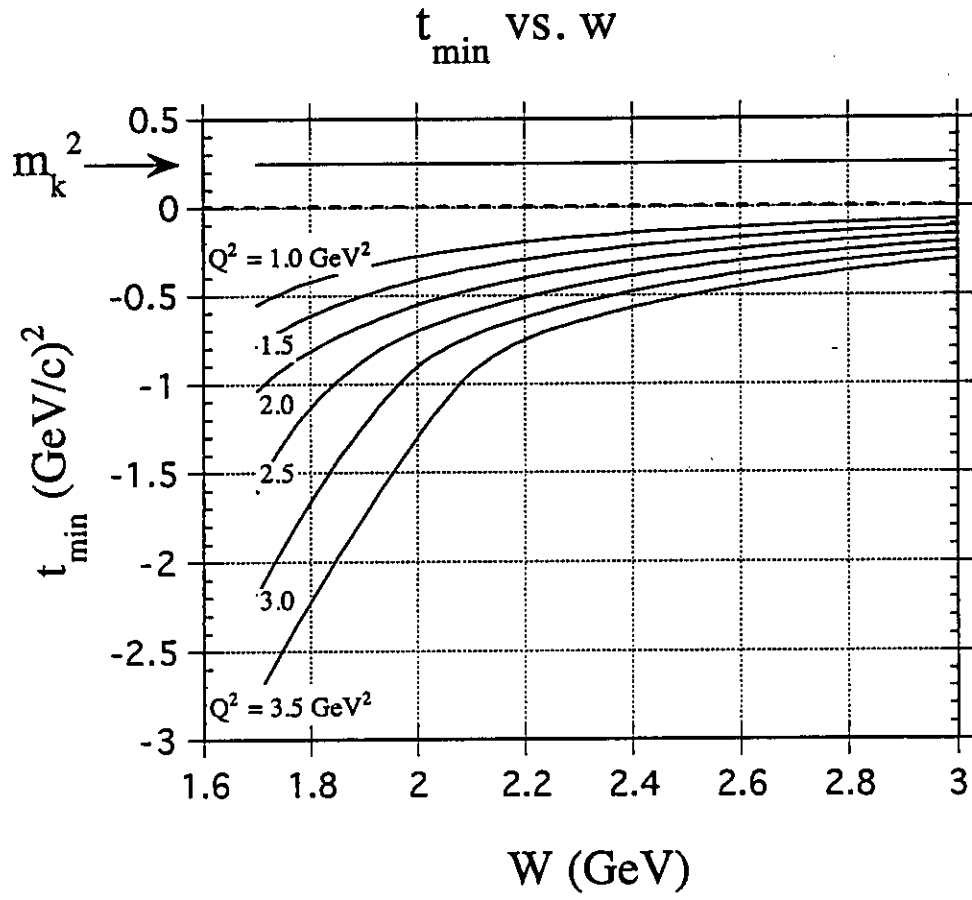


Figure 7: Loci of the minimum  $|t|$  reachable for a given  $W$  and  $Q^2$ . Each curve refers to a constant  $Q^2$  value shown in the figure.

# Kaon Form Factor

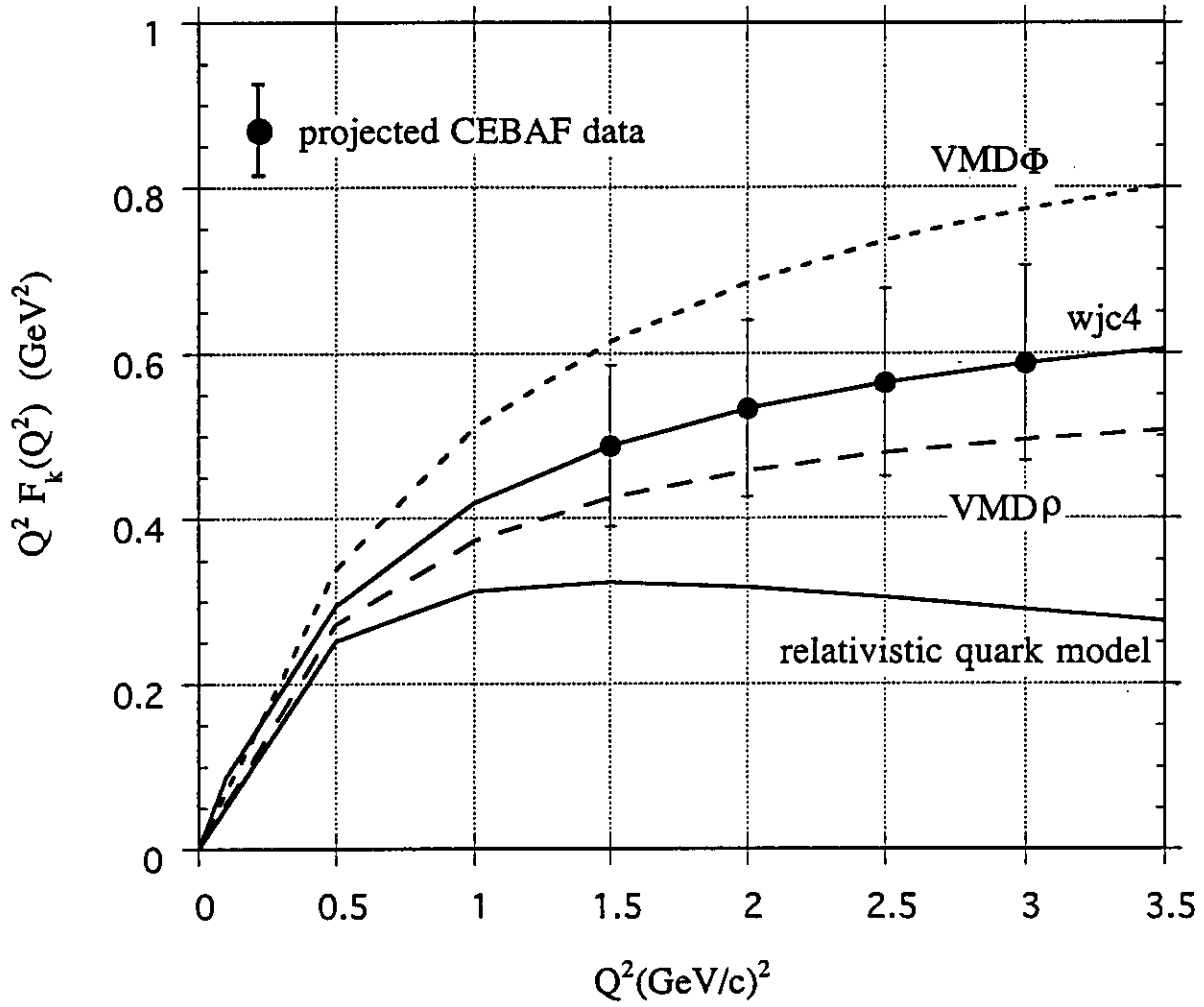


Figure 8:  $Q^2 F_K$  versus  $Q^2$ . Shown are the four points in this experiment together with the projected experimental uncertainty.



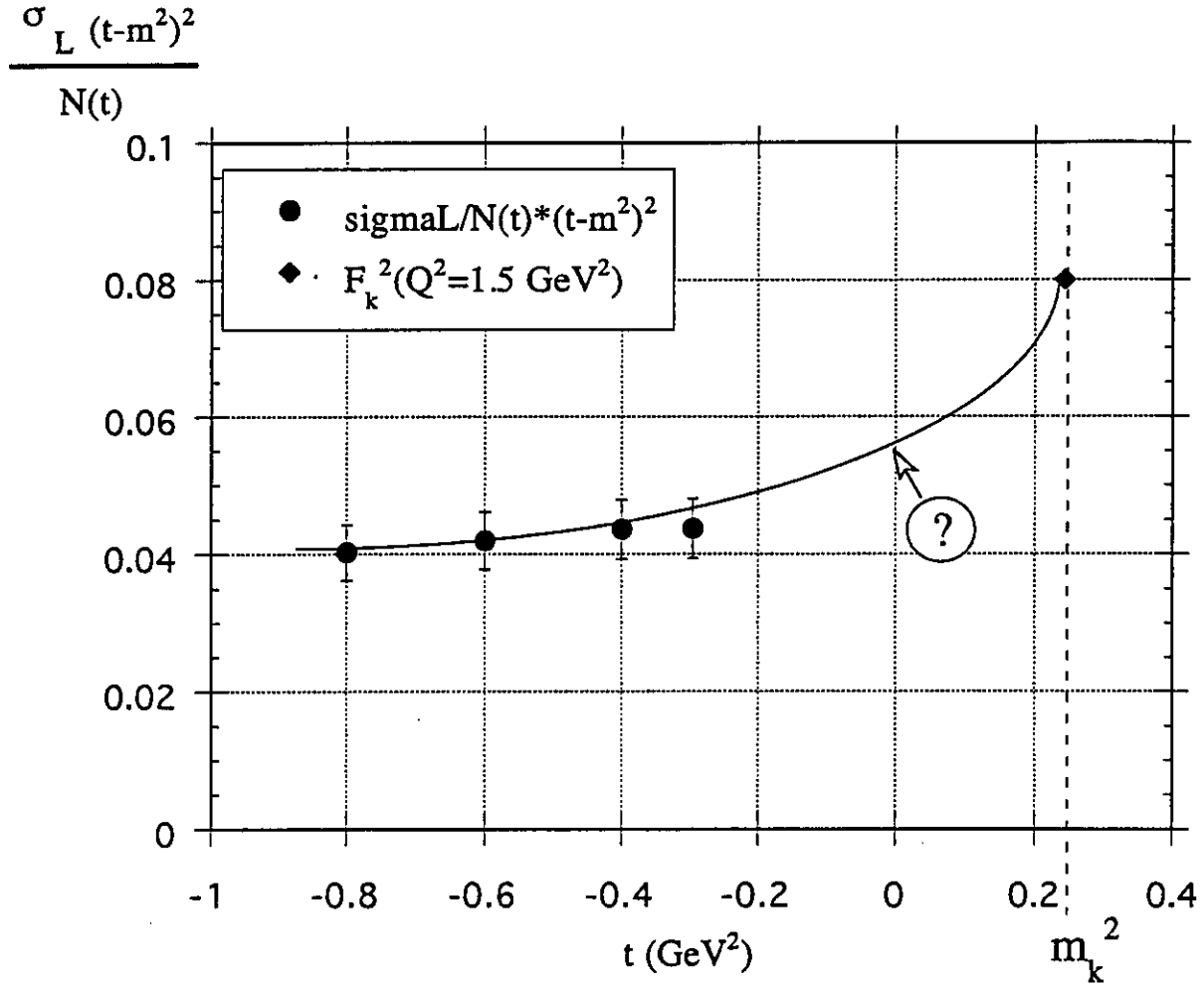


Figure 9: The  $t$ -dependence (along with the projected uncertainties) according to model wjc2, of the kaon form factor extrapolated to the pole ( $t = M_K^2$ ).

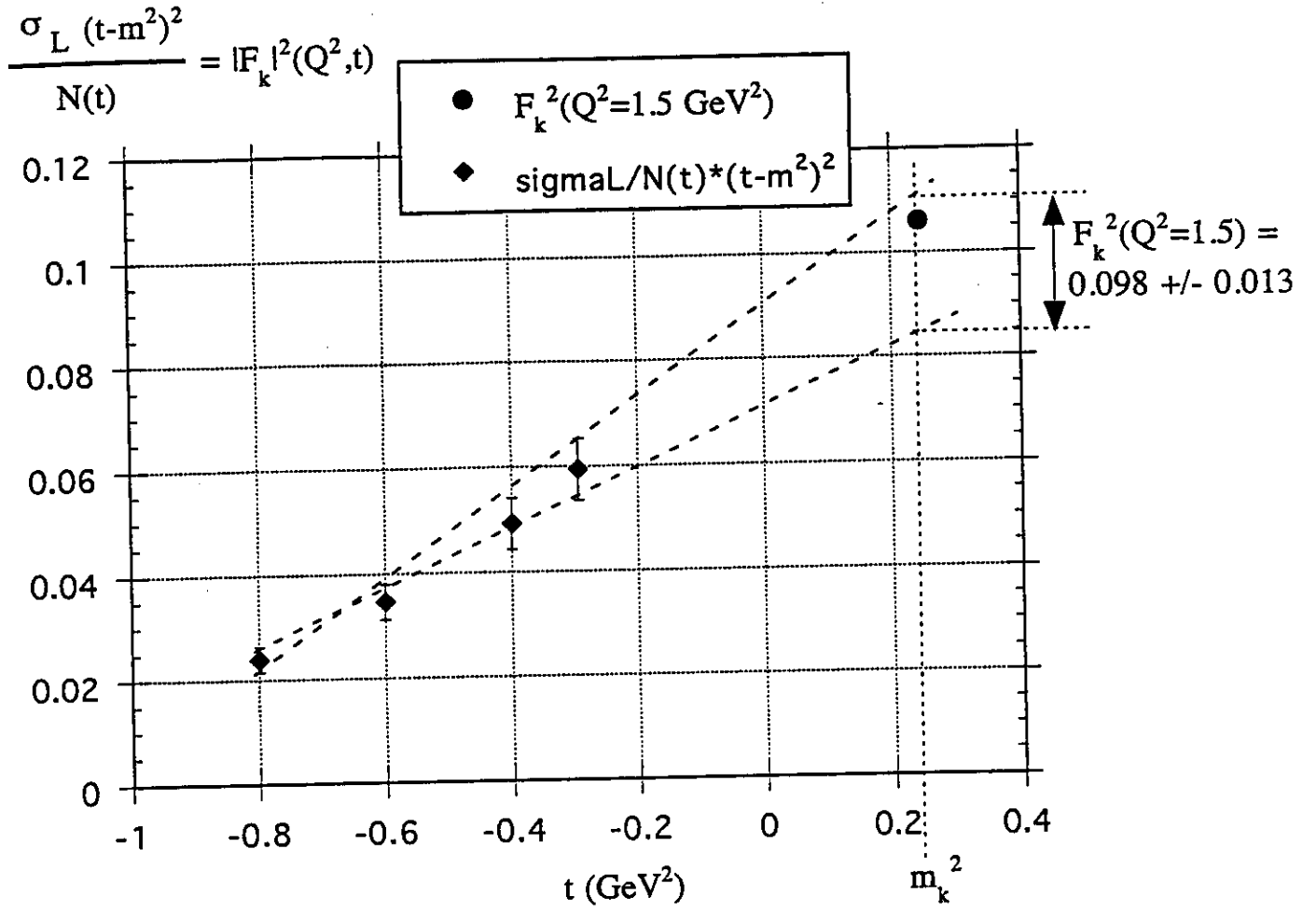


Figure 10: The  $t$ -dependence (along with the projected uncertainties) according to model wjc4, of the kaon form factor extrapolated to the pole ( $t = M_K^2$ ).

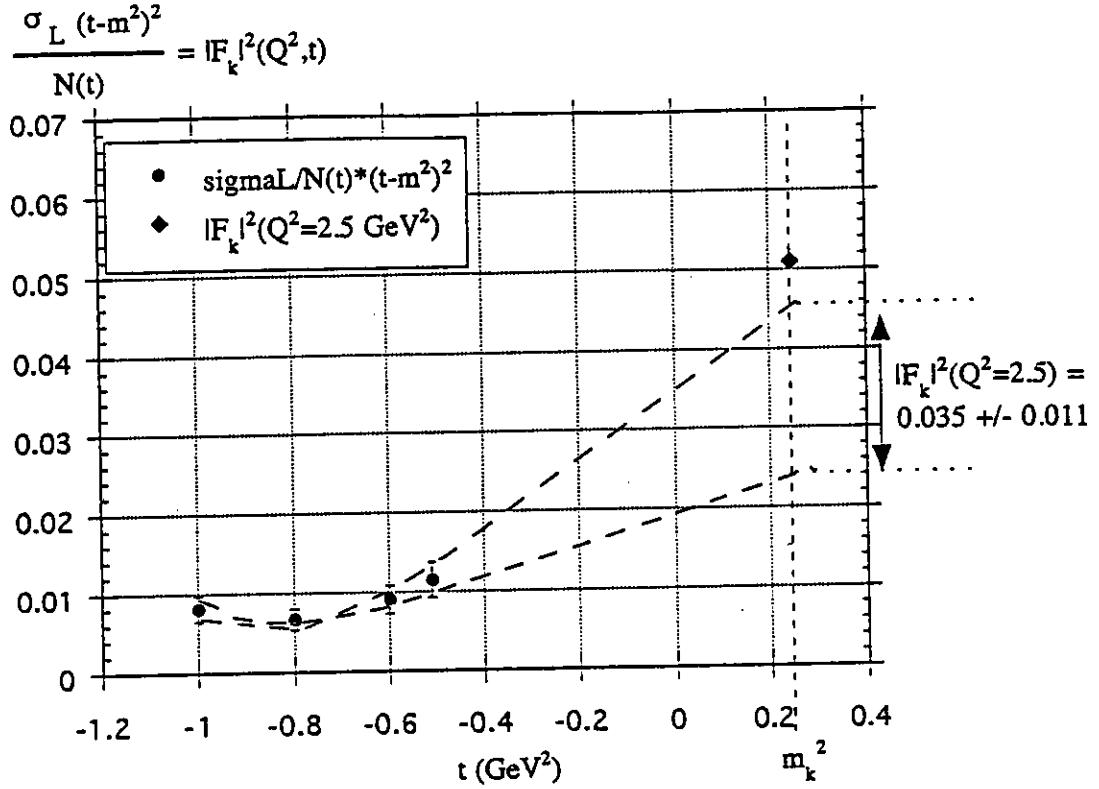


Figure 11: The  $t$ -dependence (along with the projected uncertainties) according to model wjc2, of the kaon form factor extrapolated to the pole ( $t = M_K^2$ ) for  $Q^2 = 2.5 \text{ (GeV/c)}^2$ .

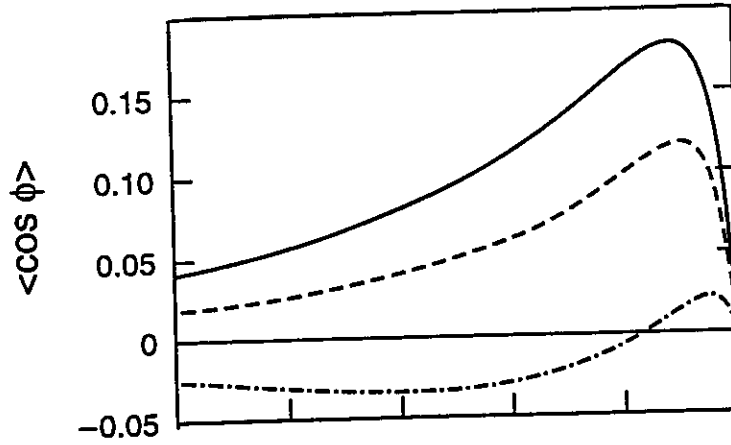


Figure 12: The asymmetry  $\langle \cos \phi \rangle$  vs.  $z$  for  $Q = 2.5 \text{ GeV}$ ,  $p_T = 0.5$  and  $k_T = 0$  (solid line), 0.25 (dashed line) and 0.5 (dash-dotted line).

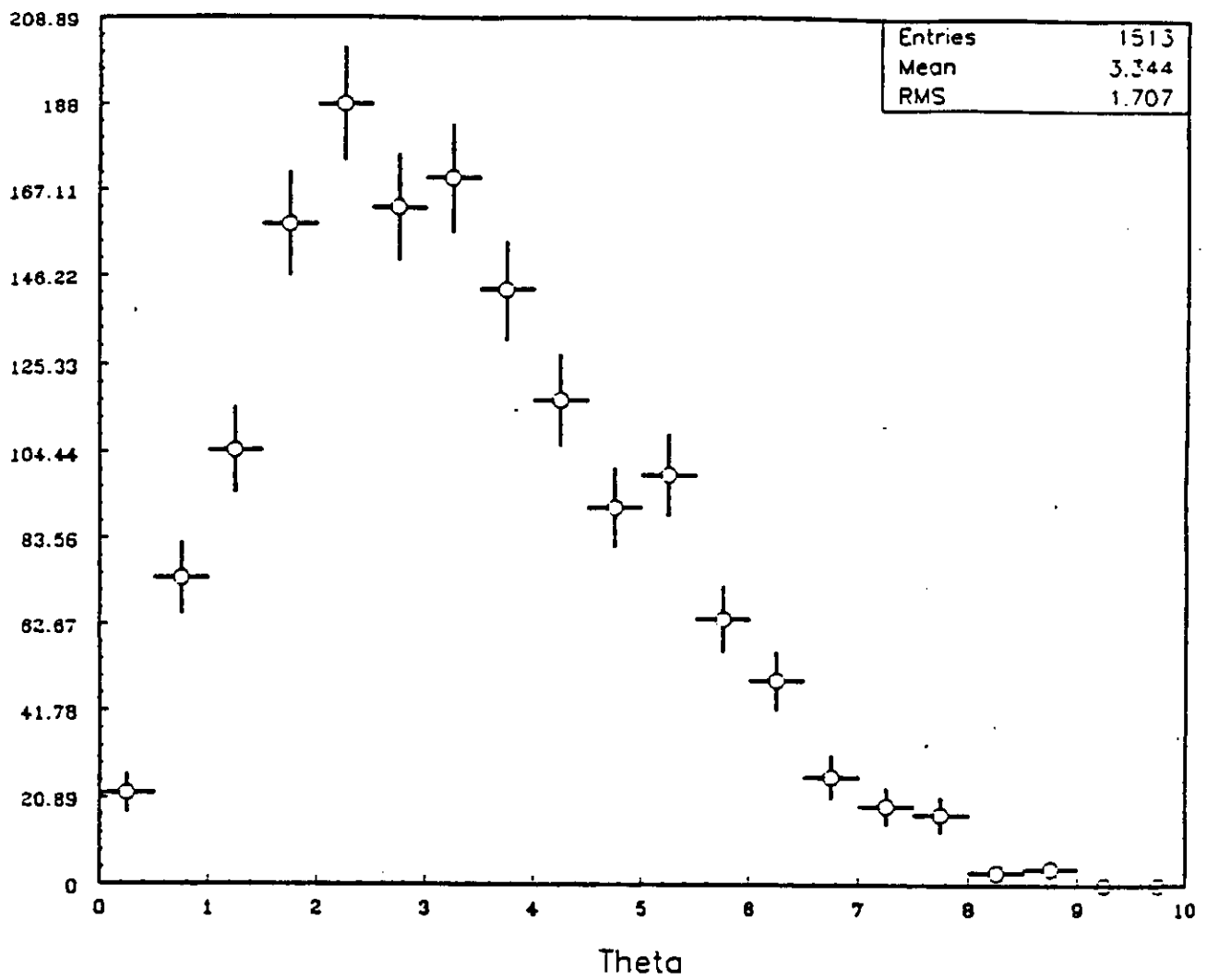


Figure 13: The yield as a function of the angle between  $\vec{q}$  and the kaon,  $\theta_{kq}$  in degrees.

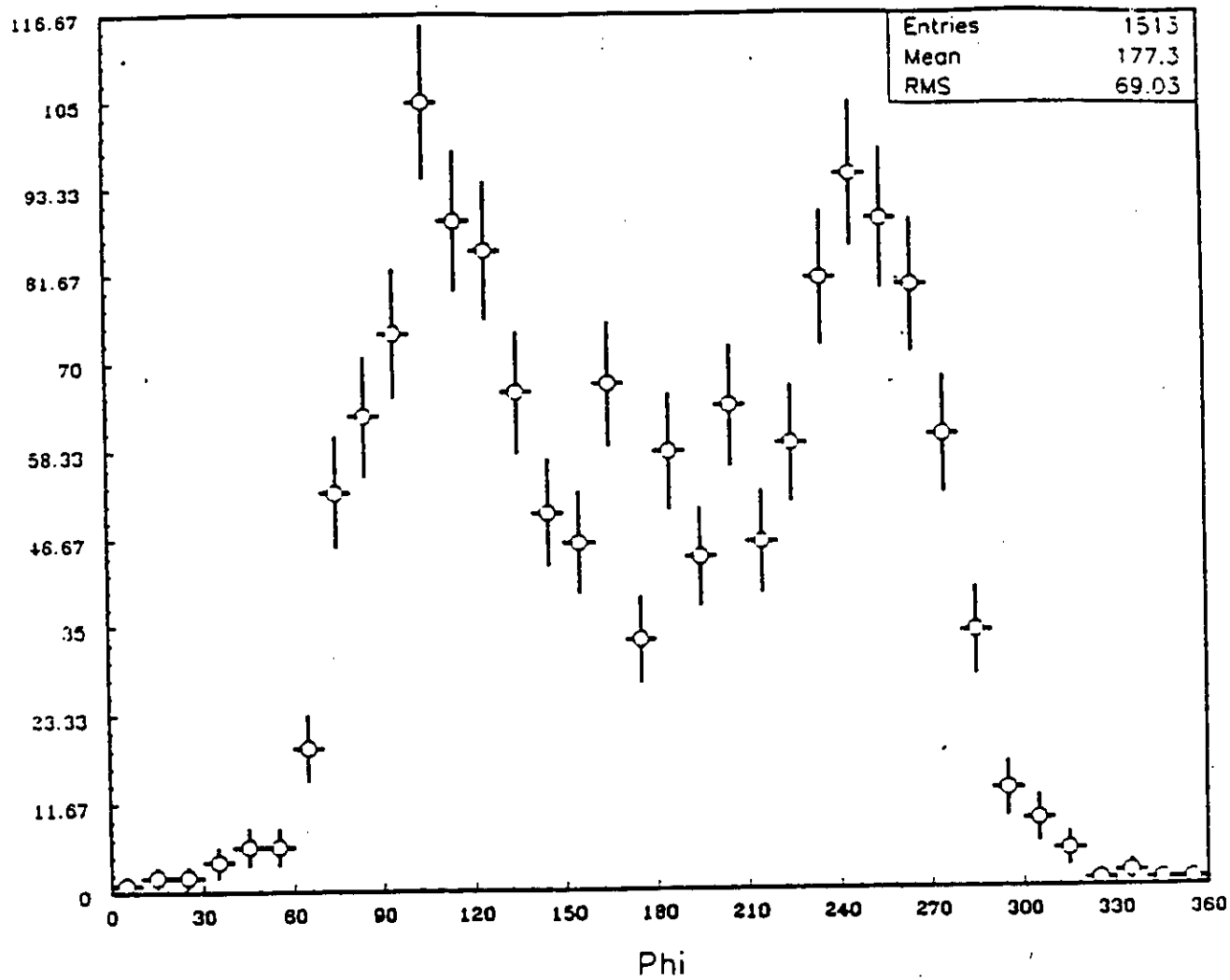


Figure 14: The yield as a function of  $\phi$ , the azimuthal angle.

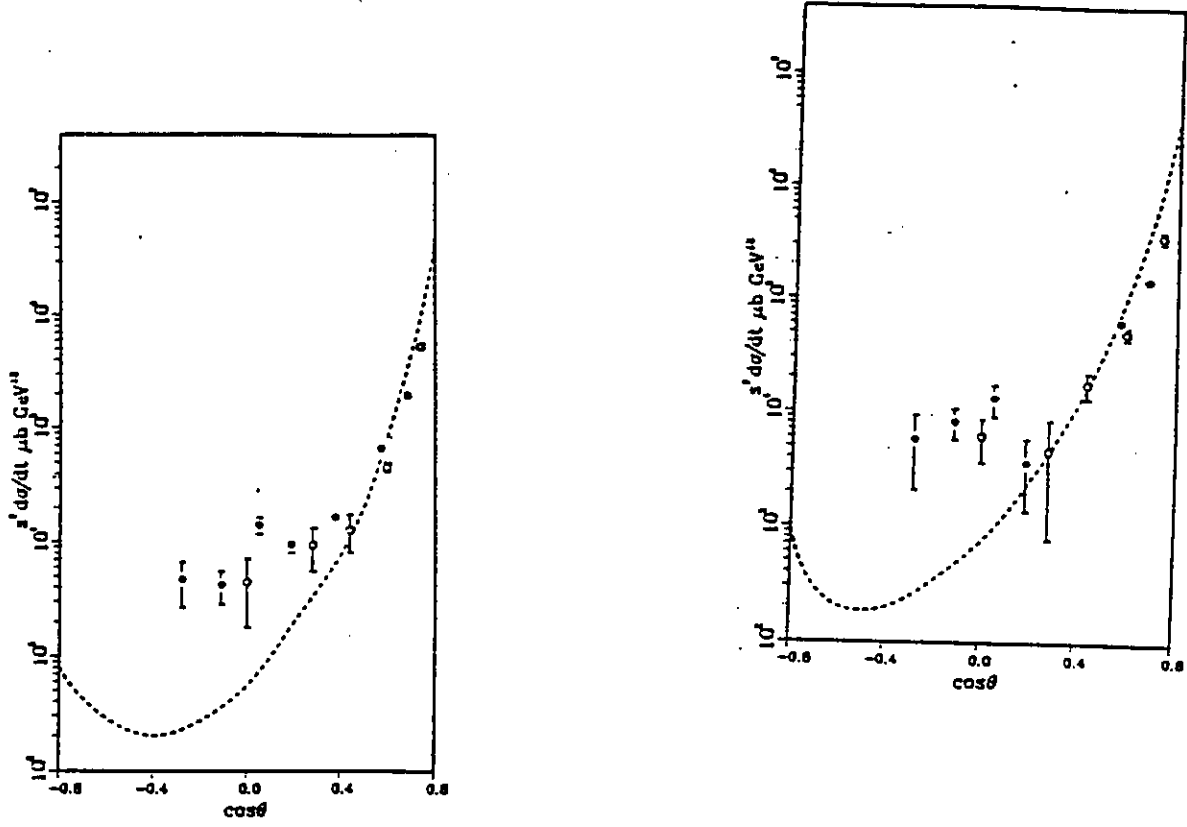


Figure 15: The a)  $\gamma p \rightarrow K^+ \Lambda$  and b)  $\gamma p \rightarrow K^+ \Sigma^0$  cross sections scaled by  $s^7$

### 3 Kinematics, Count Rates and Runtimes

#### 3.1 Kinematics

The kinematics for the longitudinal-transverse (L/T) separation are given in Table 1. The L/T separations require measuring the cross section at different values of  $\epsilon$ , the virtual photon's polarization, while centered around  $\theta_q$ , the angle of the virtual photon ( $\theta_k = \theta_q$ ). By performing the separations as a function of  $W$ , the invariant mass, and  $t$ , the hadronic momentum transfer, additional constraints will be put on the models which predict the kaon form factor. [The kaon form factor, extrapolated in  $t$ , should have only a  $Q^2$  dependence, not a  $W$  or  $t$  dependence.] The range in  $\epsilon$ , the polarization of the virtual photon, is not always as large as might be desired, the highest value limited by the 6 GeV beam and the lowest value limited by the minimum spectrometer angle (12.5 degrees). Energies of 3.6, 4.8 and 6.0 GeV were chosen as multiples of the 5-pass maximum energy. 4.0 GeV is a standard 5-pass energy, making only 5.2 GeV a non-standard energy (this point is nevertheless feasible at 4.8 GeV).

The longitudinal-transverse interference response function  $\sigma_{LT}$  will be extracted using the kinematics given in Table 2. The electron angle and momentum will be kept constant (fixing  $Q^2$  and  $W$ ) while the kaon is detected left and right of the virtual photon. By moving left and right symmetrically about the direction of the virtual photon,  $t$  was kept constant for this measurement. Subtracting the left and right measurements will separate  $\sigma_{LT}$  from the combination ( $\sigma_T + \epsilon\sigma_L + \epsilon\sigma_{TT}$ ). Counting times were minimized by performing the measurements at the same electron settings as the forward angle point of the L/T separation.

The  $t$ -dependence for the unseparated cross section will be mapped out from  $-3.0 \leq t \leq -0.3$  by changing the kaon angle and momenta, at a constant electron angle and momentum. Table 3 gives the kinematics for the  $t$ -dependence measurements. Again, counting times were minimized by performing the measurements with the electron arm at the forward angle point for the L/T separation (as it was for both the L/T separation and the  $\sigma_{LT}$ -interference measurement) and moving the kaon arm to larger angles, changing the angle between the kaon and the virtual photon. However it is no longer possible to measure both left and right of the direction of the virtual photon (as done for  $\langle \cos \phi \rangle$ ) because the measurement would require a smaller spectrometer angle than the minimum available to access the "left" kinematics.

The models predict that the transverse part of the cross section dominates at large  $|t|$ , meaning that effectively  $\sigma_T$  is being measured. The L/T separations (plotted as a function of  $t$ ) will test this hypothesis. The full cross section (as opposed to the individual response functions) will be measured in the hard scattering region.

Table 1: L/T Separation Kinematics

Kinem.	$Q^2$ (GeV/c) <sup>2</sup>	$E$ GeV	$E'$ GeV	$\theta_e$ deg	$\theta_k$ deg	$\epsilon$	$P_K$ GeV/c	$W$ GeV	$t$ GeV <sup>2</sup>
1.5a	1.5	3.6	1.54	30.12	18.87	0.644	1.46	1.8	-0.61
1.5b	1.5	6.0	3.94	14.47	24.30	0.890	1.46	1.8	-0.61
1.5c	1.5	3.6	1.14	35.22	13.81	0.496	1.99	2.0	-0.41
1.5d	1.5	6.0	3.57	15.28	19.82	0.847	1.99	2.0	-0.41
1.5e	1.5	4.8	1.89	23.46	13.79	0.636	2.51	2.2	-0.29
1.5f	1.5	6.0	3.09	16.35	16.00	0.785	2.51	2.2	-0.29
2a	2.0	3.6	1.28	38.52	17.00	0.526	1.63	1.8	-0.81
2b	2.0	6.0	3.68	17.32	23.73	0.854	1.63	1.8	-0.81
2c	2.0	3.6	0.87	47.05	12.50	0.358	2.19	2.0	-0.55
2d	2.0	6.0	3.27	18.37	19.60	0.802	2.19	2.0	-0.55
2e	2.0	4.8	1.62	29.34	13.23	0.547	2.72	2.2	-0.40
2f	2.0	6.0	2.82	19.78	15.96	0.731	2.72	2.2	-0.40
2.5a	2.5	3.6	1.01	48.98	14.55	0.396	1.79	1.8	-1.01
2.5b	2.5	6.0	3.41	20.13	22.76	0.812	1.79	1.8	-1.01
2.5c	2.5	4.0	1.01	46.44	12.50	0.372	2.38	2.0	-0.70
2.5d	2.5	6.0	3.01	21.46	18.95	0.752	2.38	2.0	-0.70
2.5e	2.5	4.8	1.36	36.08	12.50	0.451	2.93	2.2	-0.51
2.5f	2.5	6.0	2.56	23.29	15.48	0.672	2.93	2.2	-0.51
3a	3.0	3.6	0.74	63.90	12.50	0.257	1.95	1.8	-1.22
3b	3.0	6.0	3.14	23.00	21.58	0.765	1.95	1.8	-1.22
3c	3.0	4.8	1.54	37.16	14.58	0.493	2.57	2.0	-0.85
3d	3.0	6.0	3.74	24.67	18.04	0.697	2.57	2.0	-0.85
3e	3.0	5.2	1.49	36.24	12.50	0.455	3.14	2.2	-0.62
3f	3.0	6.0	2.29	27.01	14.73	0.608	3.14	2.2	-0.62

### 3.2 Cross Section Estimates and Rates

Table 4 shows the singles and coincidence rates for the L/T separation. The electron single arm rates were computed using the Monte Carlo code XSECDEEP[31] based on the SLAC deep inelastic scattering data, and averaging over the spectrometer angular and momentum acceptances. The pion rates were determined by using PIXSEC,[32] which averaged the single arm pion cross section over the spectrometer acceptances. The code computes the point cross section based on a fit to deep inelastic ( $e, \pi^-$ ) data taken at SLAC. The ( $e, \pi^+$ ) rates were assumed to be the same as the ( $e, \pi^-$ ) rates computed for the same kinematics (this is an overestimate by up to a factor of 2 of the ( $e, \pi^+$ ) rates, making it a conservative estimate). Times were calculated for  $10^4$  counts for all kinematics (except for the backward angle at  $Q^2=2.5, 3.0$  and  $W=1.8$  GeV, which were calculated for  $2.5 \times 10^3$  counts).



Table 2:  $\sigma_{LT}$  Separation Kinematics

Kinem.	$Q^2$ (GeV/c) <sup>2</sup>	$E$ GeV	$E'$ GeV	$\theta_e$ deg	$\theta_k$ deg	$\epsilon$	$P_K$ GeV/c	$W$ GeV	$t$ GeV <sup>2</sup>
1.5g	1.5	6.0	3.54	15.28	27.14	0.847	1.91	2.0	-0.55
1.5h	1.5	6.0	3.54	15.28	12.50	0.847	1.91	2.0	-0.55
2g	2.0	6.0	3.27	18.37	26.70	0.802	2.09	2.0	-0.73
2h	2.0	6.0	3.27	18.37	12.50	0.802	2.09	2.0	-0.73
2.5g	2.5	6.0	3.01	21.46	25.40	0.752	2.27	2.0	-0.89
2.5h	2.5	6.0	3.01	21.46	12.50	0.752	2.27	2.0	-0.89
3g	3.0	6.0	2.74	24.67	23.58	0.697	2.47	2.0	-1.03
3h	3.0	6.0	2.74	24.67	12.50	0.697	2.47	2.0	-1.03

Table 3:  $t$ -dependence Kinematics

Kinem.	$Q^2$ (GeV/c) <sup>2</sup>	$E$ GeV	$E'$ GeV	$\theta_e$ deg	$\theta_k$ deg	$\epsilon$	$P_K$ GeV/c	$W$ GeV	$t$ GeV <sup>2</sup>
1.5i	1.5	6.0	3.54	15.28	35.67	0.847	1.66	2.0	-1.00
1.5j	1.5	6.0	3.54	15.28	41.64	0.847	1.44	2.0	-1.40
2i	2.0	6.0	3.27	18.37	36.38	0.802	1.72	2.0	-1.40
2j	2.0	6.0	3.27	18.37	43.54	0.802	1.38	2.0	-2.00
2.5i	2.5	6.0	3.01	21.46	31.94	0.752	2.27	2.0	-1.40
2.5j	2.5	6.0	3.01	21.46	39.98	0.752	1.99	2.0	-2.20
3i	3.0	6.0	2.74	24.67	28.03	0.697	2.27	2.0	-1.40
3j	3.0	6.0	2.74	24.67	35.11	0.697	1.83	2.0	-2.20
3k	3.0	6.0	2.74	24.67	41.99	0.697	1.38	2.0	-3.00

The coincidence cross sections and rates were determined using the model wjc2[7] for  $\Lambda$  production whose analysis has been reported in chapter 2.2. For L/T separation kinematics, where  $t$  is a minimum, model wjc4 gives cross sections lower by 2–3 but, as already discussed, is less accurate in reproducing the (few) existing data at high  $Q^2$  than wjc2. [In the case of the  $t$ -dependence kinematics, as considered before, the disagreement between the models relies on the opposite slope they have.] Additionally both the  $\Sigma^0$  and the  $\Lambda(1405)$  will fall within our missing mass acceptances. The statistics will be somewhat worse due to smaller cross sections. Yields for a subset of the kinematics were also checked with the Monte Carlo code LEPTO which explicitly performs the averaging over the acceptances of both the hadron and electron arms; the two approaches gave roughly comparable rates.

Tables 5 and 6 show the rates and times for the  $\sigma_{LT}$  and  $t$ -dependence measurements (respectively). Count rates and cross sections were computed the same way as in Table 4. Shown is the total time for each setting, taking into account the kaon survival fraction for each momentum setting of the kaon spectrometer, for

Table 4: L/T Rates and counting times

Kinem.	(e,e'K) nb/GeV/sr <sup>2</sup>	(e,e'K) s <sup>-1</sup>	(e,e') s <sup>-1</sup>	(e, $\pi^-$ ) s <sup>-1</sup>	(e, $\pi^+$ ) s <sup>-1</sup>	(e,K) s <sup>-1</sup>	S/N	time hours
1.5a	0.77	0.21	$5.2 \times 10^3$	$3.9 \times 10^3$	$2.8 \times 10^4$	310	65	13
1.5b	4.04	2.88	$6.9 \times 10^4$	$4.8 \times 10^2$	$1.8 \times 10^4$	200	104	1
1.5c	0.46	0.17	$2.3 \times 10^3$	$7.9 \times 10^3$	$3.4 \times 10^4$	680	54	17
1.5d	3.19	3.66	$4.7 \times 10^4$	$1.6 \times 10^3$	$1.3 \times 10^4$	260	149	1
1.5e	0.99	0.84	$8.0 \times 10^3$	$5.5 \times 10^3$	$1.8 \times 10^4$	510	103	4
1.5f	2.33	3.24	$3.0 \times 10^4$	$2.7 \times 10^3$	$1.2 \times 10^4$	340	159	1
2a	0.33	0.10	$1.4 \times 10^3$	$3.4 \times 10^3$	$2.9 \times 10^4$	410	87	30
2b	2.00	1.66	$2.4 \times 10^4$	$2.9 \times 10^2$	$1.3 \times 10^4$	180	192	2
2c	0.18	0.06	$5.9 \times 10^2$	$1.6 \times 10^3$	$3.4 \times 10^4$	790	64	48
2d	1.58	1.93	$1.7 \times 10^4$	$6.3 \times 10^2$	$8.6 \times 10^3$	270	210	2
2e	0.45	0.36	$2.7 \times 10^3$	$3.8 \times 10^3$	$1.3 \times 10^4$	400	166	8
2f	1.16	1.62	$1.1 \times 10^4$	$1.4 \times 10^3$	$7.9 \times 10^3$	240	306	2
2.5a	0.13	0.04	$4.0 \times 10^2$	$1.4 \times 10^3$	$3.8 \times 10^4$	640	78	20*
2.5b	0.93	0.85	$9.5 \times 10^3$	$1.5 \times 10^2$	$1.0 \times 10^4$	170	263	4
2.5c	0.15	0.06	$4.3 \times 10^2$	$2.2 \times 10^3$	$2.7 \times 10^4$	710	98	44
2.5d	0.86	1.09	$7.0 \times 10^3$	$3.2 \times 10^2$	$6.5 \times 10^3$	170	457	3
2.5e	0.22	0.16	$9.4 \times 10^2$	$3.8 \times 10^3$	$1.0 \times 10^4$	340	250	18
2.5f	0.63	0.87	$4.6 \times 10^3$	$7.4 \times 10^2$	$5.6 \times 10^3$	190	497	4
3a	0.04	0.01	$1.1 \times 10^2$	$3.9 \times 10^0$	$4.8 \times 10^4$	940	48	75*
3b	0.34	0.33	$3.9 \times 10^3$	$7.8 \times 10^1$	$9.1 \times 10^3$	180	235	9
3c	0.19	0.13	$6.9 \times 10^2$	$1.2 \times 10^3$	$1.2 \times 10^4$	340	277	21
3d	0.50	0.85	$4.3 \times 10^2$	$1.2 \times 10^0$	$5.4 \times 10^3$	150	659	4
3e	0.18	0.46	$7.0 \times 10^2$	$1.9 \times 10^3$	$6.8 \times 10^3$	250	131	6
3f	0.36	0.48	$2.0 \times 10^3$	$5.1 \times 10^2$	$4.4 \times 10^3$	160	750	6

Times are for  $10^4$  counts except \* which are  $2.5 \times 10^3$  counts.

Table 5:  $\sigma_{LT}$  rates and counting times

Kinem.	(e,e'K) nb/GeV/sr <sup>2</sup>	(e,e'K) s <sup>-1</sup>	(e,e') s <sup>-1</sup>	(e, $\pi^-$ ) s <sup>-1</sup>	(e, $\pi^+$ ) s <sup>-1</sup>	(e,K) s <sup>-1</sup>	S/N	time hours
1.5g	3.00	3.19	$4.7 \times 10^4$	$1.6 \times 10^3$	$2.4 \times 10^3$	45	756	1
1.5h	2.65	2.82	$4.7 \times 10^4$	$1.6 \times 10^3$	$7.2 \times 10^4$	1350	22	1
2g	1.49	1.69	$1.7 \times 10^4$	$6.3 \times 10^2$	$1.4 \times 10^3$	31	1600	2
2h	1.28	1.46	$1.7 \times 10^4$	$6.3 \times 10^2$	$6.0 \times 10^4$	1310	32	2
2.5g	0.82	0.97	$7.0 \times 10^3$	$3.2 \times 10^2$	$1.0 \times 10^3$	25	2700	3
2.5h	0.70	0.82	$7.0 \times 10^3$	$3.2 \times 10^2$	$4.8 \times 10^4$	1180	49	4
3g	0.49	0.59	$4.3 \times 10^2$	$1.2 \times 10^0$	$9.3 \times 10^2$	26	26000	5
3h	0.42	0.51	$4.3 \times 10^2$	$1.2 \times 10^0$	$3.5 \times 10^4$	963	615	6

Table 6:  $t$ -dependence rates and counting times

Kinem.	(e,e'K) nb/GeV/sr <sup>2</sup>	(e,e'K) s <sup>-1</sup>	(e,e') s <sup>-1</sup>	(e, $\pi^-$ ) s <sup>-1</sup>	(e, $\pi^+$ ) s <sup>-1</sup>	(e,K) s <sup>-1</sup>	S/N	time hours
1.5i	2.27	1.88	$4.7 \times 10^4$	$1.6 \times 10^3$	$9.1 \times 10^2$	14	1400	2
1.5j	1.66	1.02	$4.7 \times 10^4$	$1.6 \times 10^3$	$8.9 \times 10^2$	10	1000	3
2i	1.03	0.85	$1.7 \times 10^4$	$6.3 \times 10^2$	$5.4 \times 10^2$	9	2700	4
2j	0.65	0.34	$1.7 \times 10^4$	$6.3 \times 10^2$	$8.7 \times 10^2$	9	1100	9
2.5i	0.66	0.64	$7.0 \times 10^3$	$3.2 \times 10^2$	$7.8 \times 10^1$	2	22000	5
2.5j	0.40	0.25	$7.0 \times 10^3$	$3.2 \times 10^2$	$2.6 \times 10^1$	1	17000	12
3i	0.43	0.46	$4.3 \times 10^2$	$1.2 \times 10^0$	$3.7 \times 10^2$	9	60000	6
3j	0.29	0.22	$4.3 \times 10^2$	$1.2 \times 10^0$	$4.0 \times 10^2$	7	28000	13
3k	0.17	0.07	$4.3 \times 10^2$	$1.2 \times 10^0$	$1.2 \times 10^3$	12	9000	38

both the singles rates and the coincidence rates. [The kaon momentum ranges from 1.4 GeV/c to 3.1 GeV/c, corresponding to 10–36% survival fractions for the HRS flight path.] Count rates assume an incident beam current of 100  $\mu$ A, on a 10 cm LH2 target, and a 7.8 msr solid angle for each HRS2 spectrometer.

The signal-to-noise ratio was computed by computing the kaon single arm (e,K) rates using the procedure suggested in [33], and using a 2 ns resolving time. The kaon single arm rates were averaged over the spectrometer angular acceptances and the survival fraction of the kaons was taken into account at each spectrometer setting. No cuts on missing mass were assumed in calculating the signal-to-noise.

## 4 Detector Performance and Error Analysis

### 4.1 Particle Identification

Clean particle identification of the kaon is crucial for this experiment. Particle identification in the hadron arm will be made using the combination of the time-of-flight technique and the Čerenkov counters (aerogel and gas) operated in the threshold mode. The time-of-flight technique makes use of the 28 meter flight path of the HRS to differentiate between kaons, pions and protons up to momenta of 2 GeV/c, as shown in Figure 16. The TOF will be started on the correct beam bucket (identified by electron TOF) and stopped on a particle in the final scintillator. Above 2 GeV/c, TOF will only be useful in separating between kaons and protons.

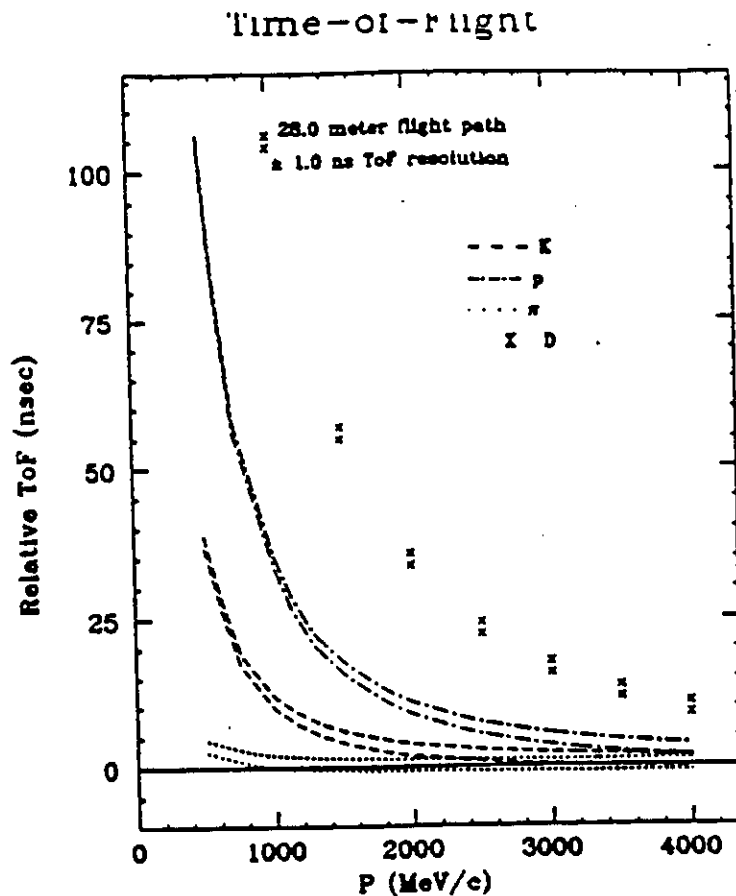


Figure 16: Relative Time-of-Flight with a 2 ns FWHM timing resolution.

Čerenkov counters in the hadron arm will differentiate between pions, kaons and protons at all incident momenta listed in this proposal. The Čerenkov counters will also enable us to reject pions resulting from kaons which decay during the trip

Table 7: L/T Separation Statistical Uncertainty

Kinem.	$Q^2$ (GeV/c) <sup>2</sup>	$\sigma_T$ nb/sr	$\Delta\sigma_T$ %	$\sigma_L$ nb/sr	$\Delta\sigma_L$ %
1.5a-b	1.5	105.3	9.5	62.0	23.0
1.5c-d	1.5	117.8	3.6	53.2	11.4
1.5e-f	1.5	118.2	5.2	32.1	28.0
2a-b	2.0	79.6	7.2	53.0	15.0
2c-d	2.0	89.1	2.5	43.6	7.7
2e-f	2.0	89.8	3.6	25.6	17.4
2.5a-b	2.5	63.2	6.4	44.2	19.0
2.5c-d	2.5	70.6	2.6	35.5	11.1
2.5e-f	2.5	67.1	2.4	14.9	14.3
3a-b	3.0	51.9	6.7	36.9	18.3
3c-d	3.0	57.9	5.8	29.2	14.2
3e-f	3.0	46.0	2.6	4.8	30.0

through the spectrometer. Figure 17 (taken from the CEBAF CDR) shows the velocity of particles (plotted as  $1-\beta$ ) versus momentum and the indices of refraction at STP (plotted as  $n-1$ ).

The electron arm will have time-of-flight, Čerenkov counters, and shower counters to distinguish  $e^-$  from  $\pi^-$  and  $K^-$ . The  $K^-$  singles rate is much smaller than the  $\pi^-$  singles rate meaning that the Čerenkov counters and shower counts will suffice. Operated in the threshold mode, the Čerenkov counter is expected to give pion rejection rates of upto  $10^3$ . The dominant background (knock-on electrons) will be reduced another 2 orders of magnitude by the lead-glass shower counters giving a total pion rejection ratio of  $\geq 10^5$  – higher than required for this experiment.

## 4.2 Statistical Uncertainties

The fraction of the  $(e, e' K^+)$  final states which have only a single  $\Lambda$  in them ranges between 50–60% over our kinematics; the fraction of  $(e, e' K^+)$  final states which have only a single  $\Sigma^0$  in them are approximately 15% of the total number. The remainder are continuum states with more than 1 particle or higher resonances. The statistics will allow the measurement of (for the  $(e + p \rightarrow e' + K^+ + \Lambda)$  channel) the full cross section with a 1% statistical uncertainty; the statistical uncertainty on the extracted values of  $\sigma_L$  and  $\sigma_T$  is given in Table 7. [The  $(e + p \rightarrow e' + K^+ + \Sigma^0)$  channel will have statistical uncertainties approximately twice as large.] Tables 8 and 9 show the uncertainties for the  $\langle \cos \phi \rangle$  and  $t$ -dependence kinematics, respectively.

Table 8:  $\langle \cos \phi \rangle$  Asymmetry Statistical Uncertainty

Kinem.	$Q^2$ (GeV/c) <sup>2</sup>	$A$	$\Delta A$ %	$\Delta\sigma_{LT}$ %
1.5g-h	1.5	0.062	4.0	7.0
2g-h	2.0	0.076	3.6	6.0
2.5g-h	2.5	0.079	3.5	5.8
3g-h	3.0	0.077	3.6	5.5

Table 9:  $t$ -dependence Statistical Uncertainty

Kinem.	$Q^2$ (GeV/c) <sup>2</sup>	$t$ GeV <sup>2</sup>	$d\sigma_v/d\Omega_k$ nb/GeV/sr <sup>2</sup>	$\Delta d\sigma_v/d\Omega_k$ %
1.5i	1.5	-1.00	2.27	1.0
1.5j	1.5	-1.40	1.66	1.0
2i	2.0	-1.40	1.03	1.0
2j	2.0	-2.00	0.65	1.0
2.5i	2.5	-1.40	0.66	1.0
2.5j	2.5	-2.20	0.40	1.0
3i	3.0	-1.40	0.43	1.0
3j	3.0	-2.20	0.29	1.0
3k	3.0	-3.00	0.17	1.0

Table 10: Systematic Relative Uncertainties

Scattering Angles	1.0%
Target Density Variations	0.5%
Cell Walls	0.5%
$K^+$ absorbtion	0.5%
Detector Inefficiencies	2.0%
Kaon Decay	0.5%
Radiative Corrections	0.5%
Beam Current	1.0%
Acceptances	1.0%
Total	2.9 %

### 4.3 Systematic Uncertainties

The systematic uncertainties contribute differently to the three types of measurements. The systematical uncertainties which are most important however are the relative errors, not the absolute uncertainties since the physics will be extracted by comparing measured cross sections. The absolute normalization of the data set requires the absolute uncertainty.

Shown in Table 10 are the contributions to the extracted response functions of the RELATIVE uncertainties between successive measurements.

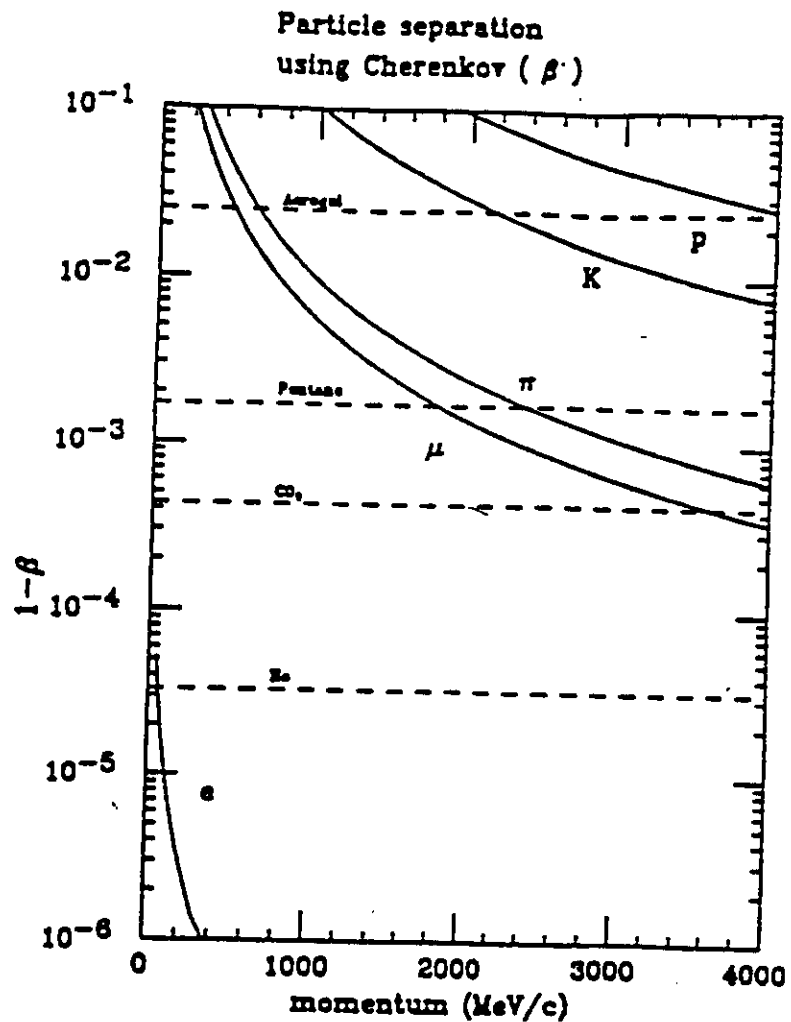


Figure 17: The the velocity of particles (plotted as  $1-\beta$  versus momentum and the indices of refraction at STP, plotted as  $n-1$ , of several materials used in Čerenkov counters.



## 5 Runplan and Beamtime Summary

Table 11: Beam Time Summary

Set-up/Check-out	50 hours
DAQ for L/T separations	343 hours
DAQ for $\sigma_{LT}$	24 hours
DAQ for $t$ -dependence	92 hours
Angle Changes	41 hours
Empty Target	10 hours
Total	560 hours

The beam time summary is reported in Table 11. The additional time needed for overhead is fairly small: angle changes are estimated to total 41 hours, 50 hours of set-up and check out is required, and short empty target run at each setting gives another 10 hours. Added with the 459 DAQ hours and an unknown amount of time for energy changes, the total beam time request of 560 hours as shown in Table 4, plus the time needed to perform the 3 energy changes. To minimize overhead, it is assumed that all points at a given incident energy will be measured, moving the spectrometer accordingly, before changing energies. In particular, the  $\sigma_{LT}$  response function and the  $t$ -dependence will be measured before changing the electron angle or momentum to minimize the systematic uncertainties.

As can be seen from Tables 4-6, the signal-to-noise is excellent at all kinematics. The rates in the focal plane of the spectrometers are low, meaning we could run with higher luminosity if it was available. The cuts on the missing mass spectrum will be done in replay, not the trigger, enabling one to obtain data on additional exclusive channels. [No estimates were given for the statistical uncertainties associated with these additional channels because of the small yields involved.] The signal-to-noise for particular final state will be larger than for the entire spectrum.

Pion data will be taken in prescale mode. This is important not only to tell us the shape of the backgrounds, but also because many of the physics arguments given are general to pseudo-scalar meson production. The use of the pion final states will provide additional constraints on the theory. The pion coincidence rates are considerably higher than the kaon rates; the statistical uncertainty will be less important.

## References

- [1] R. A. Adelseck, B. Saghai, Phys. Rev. C 42 108 (1990).
- [2] P. Feller, et. al., Nucl. Phys. B39 413 (1979).
- [3] M. Bockhurst *et al.*, Contributed Paper, Few Body XIV, 551 (1994).
- [4] P. Brauel *et al.*, Z. Physik, 3, 101 (1979).
- [5] A. Bodek *et al.*, Phys. Lett. 51B, 417 (1974).
- [6] J. Ashman *et al.*, Nucl. Phys. B328, 1 (1989).
- [7] R. A. Williams, C-R Ji and S. R. Cotanch, Phys. Rev. C 46 1617 (1992).
- [8] C.B. Dover, G.E. Walker, Phys. Rep. 89 1 (1982).
- [9] J. Adam, J. Mares, O. Richter, M. Sotona, S. Frullani, Czech. J. Phys. 42 1167 (1992).
- [10] L. S. Celenza, A. Pantirix, C. M. Shakin, and Hui-Wen Wang, Phys. Rev. C 41 366 (1990).
- [11] G.R. Farrar *et al.*, Nucl. Phys. B349, 655 (1991).
- [12] M. Schuermann, Thesis, Wuppertal University (1992).
- [13] T. Azemoon *et al.*, Advance in Nucl. Phys. 17, 47 (1987).
- [14] S. Frullani, G. Garibaldi, F. Ghio, M. Iodice, G.M. Urciouli, R. DeLeo, Multi Purpose Sepctrometer, INFN-ISS 90/5, (1990).
- [15] R. G. Arnold *et al.*, Phys. Rev. Lett., 52, 727 (1984).
- [16] S. R. Cotanch and S. S. Hsiao, Nucl. Phys. A 450 4192 (1986).
- [17] C-R Ji and S. R. Cotanch, Phys. Rev. D 41 2319 (1990).
- [18] R.A.Williams, C.R.Ji, S.R.Cotanch., Phys. Rev. D 41 1449 (1990).
- [19] C. J. Bebek *et al.*, Phys. Rev. D 15, 47 (1977).
- [20] T. Sjöstrand, Comp. Phys. Commun. 39, 347 (1986).
- [21] F. S. Dietrich and C. W. Johnson, Proc. of the 1986 CEBAF Summer Study, RPAC II, 389 (1986).
- [22] B. Andersson *et al.*, Phys. Rep. 97, 31 (1983).

- [23] O.K. Baker, CEBAF Experimental Proposal 91-022 (1991).
- [24] O.K. Baker, Hampton University HUPHY-03-92 (1992).
- [25] R.C.E. Devenish, D.H. Lyth, Phys. Rev. D 5 47 (1972).
- [26] E.B. Dally et. al., Phys. Rev. Lett. 45 232 (1980).
- [27] F. Cardarelli et. al., Phys. Lett. B 332 1 (1994) and F. Cardarelli et al. "Proceedings of Workshop on CEBAF at Higher Energies", Editors: N.Isgur, P.Stoler, (1994).
- [28] R. N. Cahn, Phys. Lett. 78B, 269 (1978).
- [29] E. L. Berger, Z. Phys. C4, 289 (1980).
- [30] A. Brandenburg, V.V. Khoze, D. Müller, SLAC-PUB-6688 (1994).
- [31] C. C. Chang, computer code XSECDEEP, private communication (1993).
- [32] C. C. Chang and P. Markowitz, computer code PIXSEC, private communication (1993).
- [33] C.E. Hyde-Wright, W. Bertozzi, J.M. Finn, Proc. of the 1985 CEBAF Workshop, Newport News, Virginia (1985).
- [34] R. E. Taylor, Proc. 4<sup>th</sup> Symp. on Electron and Photon Interactions, Liverpool, Daresburg Nucl. Phys. Lab. 251 (1969).
- [35] C. C. Chang AIP 269 51 460 (1992).
- [36] S. J. Brodsky, Plenary Talk, Workshop on CEBAF at Higher Energies, (1994).
- [37] F. Schlumpf, SLAC-PUB-6483 (1994).
- [38] A. Calogeracos, N. Dombey, G. West, LA-UR-93-115 (1994).

## Appendix: Participants

O.K. Baker	G. Kumbartzki
E. Beise	J.J. Kelly
W. Bertozzi	R. De Leo
E. Brash	J. LeRose
H. Breuer	G.J. Lolos
C.C. Chang	R. Lourie
N.S. Chant	K. Maeda
J.P. Chen	P. Markowitz
E. Cisbani	S. Nanda
F. Duncan	Z. Papandrea
J.M. Finn	R. Perrino
S. Frullani	R. Ransome
F. Garibaldi	P.M. Rutt
A. Gasparian	P.G. Roos
S. Gilad	A. Saha
S. Glamazdin	T. Saito
J. Gomez	A. Sarty
C. Glashausser	R. Gilman
G.M. Huber	G.M. Urciuoli
M. Iodice	H. Voskanian
S. Beedoe	B. Wojosetkhowski